ANL-7664

Argonne National Laboratory

DYNAMIC SIMULATION AND ANALYSIS OF EBR-II ROD-DROP EXPERIMENTS

by

A. V. Campise

Printed in the United States of America
Available from
National Technical Information Service
U.S. Department of Commerce
Springfield, Virginia 22151
Price: Printed Copy $3.00; Microfiche $0.65

ANL-7664
Reactor Technology

ARGONNE NATIONAL LABORATORY
9700 South Cass Avenue
Argonne, Illinois 60439

DYNAMIC SIMULATION AND ANALYSIS OF EBR-II ROD-DROP EXPERIMENTS

by

A. V. Campise

EBR-II Project

March 1970

TABLE OF CONTENTS

TABLE OF CONTENTS

LIST OF FIGURES

LIST OF FIGURES

LIST OF FIGURES

LIST OF TABLES

DYNAMIC SIMULATION AND ANALYSIS OF EBR-II ROD-DROP EXPERIMENTS

by

A. V. Campise

ABSTRACT

The neutronic, thermal, and hydraulic characteristics of EBR-II were modeled with the AIROS-IIA[1] dynamic-simulation program. The radial power and reactivity distributions in core and blanket regions were simulated by dividing the core and inner blanket into individual feedback channels, each representing an average fuel element in various rows of the reactor. Average power and flow rates were used to compute the temperature transients associated with rod-drop experiments; in turn, these temperatures were used with weighted temperature coefficients to compute the many temperature-induced reactivity feedbacks. These computations were applied to recent EBR-II power runs in which rod-drop experiments had been conducted; the computed results showed very good agreement with experimental data on power level and reactivity feedback for the first 40 sec following the rod drops. The dynamic-simulation model describes the response of the reactor for the first 40 sec as being due primarily to driver-fuel axial expansion and to density changes in the sodium coolant. These two sources of reactivity feedback appear to be sufficient to explain the variations measured in the rod-drop experiments.

The dynamic-simulation model was also used to analyze EBR-II cores having a stainless steel reflector. A one-parameter variation study was conducted with all computed negative temperature coefficients held constant and a single positive feedback assumed to be due to reverse bowing in the stainless steel reflector. The computed results agree fairly well with measured rod-drop data and also with measured power-coefficient data from these cores.

I. INTRODUCTION

Control, stability, and safety of EBR-II are of primary importance in the successful operation of this LMFBR fast-neutron irradiation facility.* A continuing safety surveillance is maintained through the use of rod-drop techniques. Periodic testing of the reactor is accomplished by rod-drop experiments with a stainless steel rod in place of a standard control rod. A data-acquisition system is used to reduce the data, and an inverse kinetics digital program is used to compute the reactivity feedback associated with the power variation recorded from an out-of-core ion chamber. The feedback data comprise the basic experimental results relating to the reactor stability and to the dynamic characteristics of a particular core loading.

Various modeling techniques[2,3] have been used to understand the characteristics of the feedback data from various EBR-II core loadings. The approach formulated in this report is that of a dynamic simulation of the reactor core and rod-drop experiment. Radial and axial heat-transfer nodes are set up to compute the temperature distributions in "averaged" fuel elements in various rows of the reactor core and inner blanket. Prompt- and delayed-neutron constants are used as input to the basic space-independent reactor-kinetics equations to solve the power variation resulting from a given rod drop. A closed-loop reactivity feedback network is maintained, and temperature changes in the fuel and coolant are associated with the weighted and localized temperature coefficients of reactivity. The temperature-induced reactivity changes are used to compute the total reactivity feedback associated with a given rod-drop experiment.

The dynamic simulation, as outlined above, is based on fundamental principles of reactor kinetics and heat transfer as applied to data from the rod-drop experiments. The AIROS-IIA code[1] is used to program the neutronic, thermal, and hydraulic characteristics of each EBR-II core loading. A complete description of the theoretical model and the input data is given in the following section.

*Experimental Breeder Reactor II (EBR-II) is the United States Atomic Energy Commission's primary facility for irradiation tests for its Liquid Metal Fast Breeder Reactor (LMFBR) program.

II. THEORETICAL MODEL

The reactor core and inner blanket are divided into eight "averaged" rows, seven in the core and one in the inner blanket. Corresponding to these rows are six feedback channels that represent driver fuel. A seventh channel is used to represent the control-rod locations and to compute the reactivity feedback of the control rods in the closed-loop feedback network. The eighth feedback channel represents the inner blanket.

Figure 1 is a schematic representation of the eight feedback channels used to represent the EBR-II core and inner blanket. Figure 2 shows the basic feedback network used to simulate the closed-loop behavior of EBR-II. As indicated in Fig. 2, an "averaged" fuel element is taken to simulate each row of the reactor core, and also one is taken for the control rods. The final channel is associated with inner-blanket material.

The basic reactivity equation is

$$\rho(t) = -\alpha t + \sum_{K=1}^{NF} F_K(\delta T)_K, \qquad (1)$$

where

$\rho(t)$ = the total reactivity feedback of the system;

α = the reactivity ramp rate associated with the stainless steel drop rod in \$/sec;

t = the time in seconds;

F_K = the weighted temperature coefficient of reactivity associated with feedback node K;

$(\delta T)_K$ = the temperature change in feedback node K;

NF = the total number of feedback nodes in the closed loop;

and

K = the index of the number of feedback nodes.

Ninety-six different feedback nodes (12 for each of the eight channels) are considered in the EBR-II dynamic-simulation model. In each channel, these nodes consist of nine in fuel (or blanket) material, and three in sodium coolant. (As Fig. 1 shows, the model has 19 nodes per channel, but seven of these--three in cladding, three in sodium bond, and one in inlet sodium coolant--are not considered feedback nodes.)

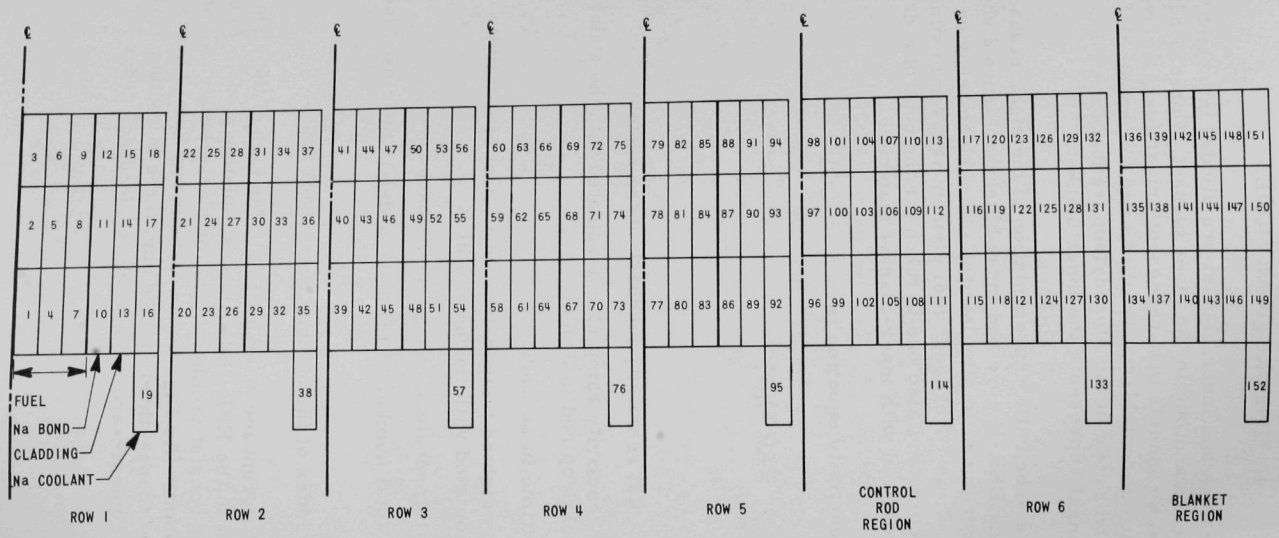

Fig. 1. Eight-channel Representation of EBR-II Core and Blanket for Feedback Modeling

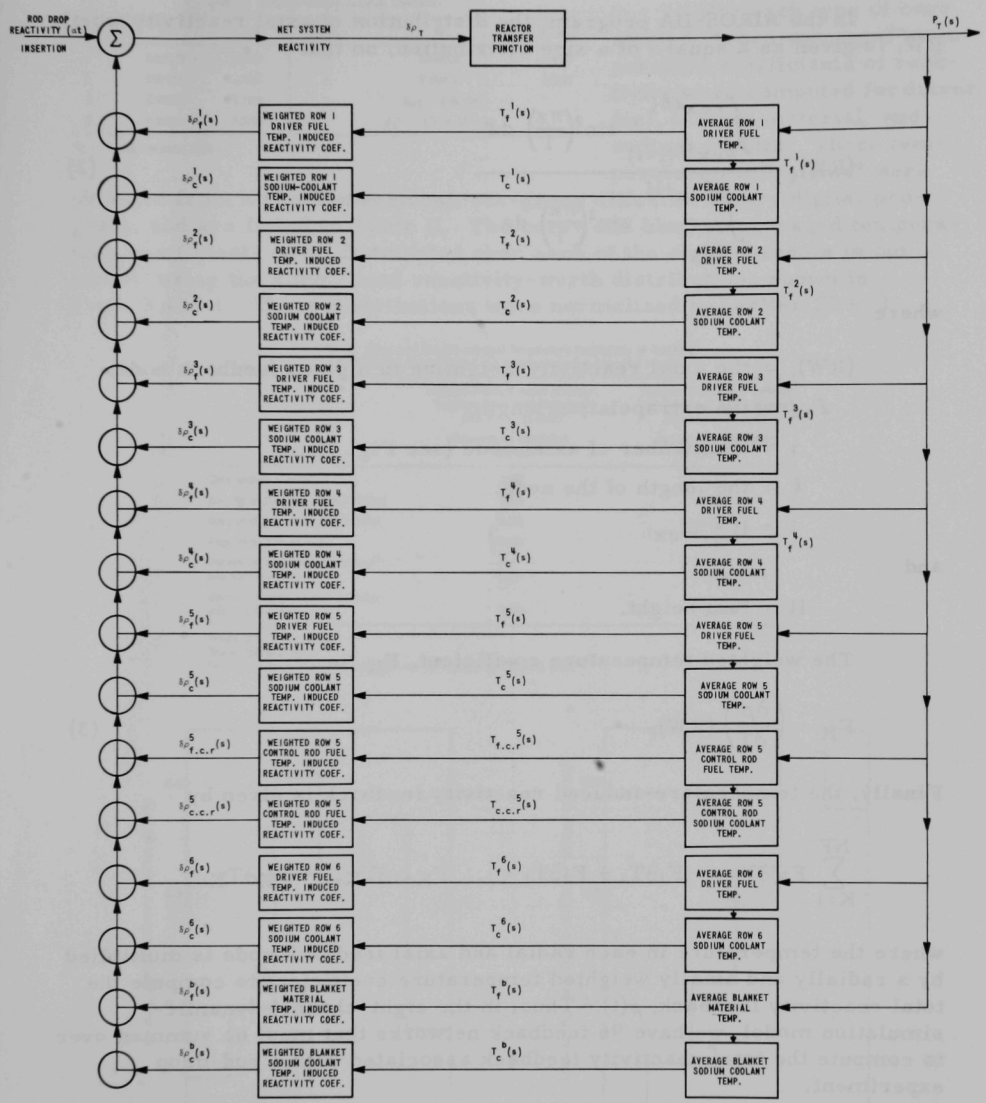

Fig. 2. Feedback Network for Simulating the Closed-loop Behavior of EBR-II

In the AIROS-IIA program, the distribution of axial reactivity worth, RW, is given as a square of a sine distribution, so that

$$(RW)_i = \frac{\int_{\ell_{ex}+\ell(i-1)}^{\ell_{ex}+\ell_i} \sin^2\left(\frac{\pi z}{l}\right) dz}{\int_{\ell_{ex}}^{\ell_{ex}+H} \sin^2\left(\frac{\pi z}{l}\right) dz}, \qquad (2)$$

where

$(RW)_i$ = the axial reactivity weighting in a given feedback node;

ℓ_{ex} = the extrapolation length;

i = the number of axial node (see Fig. 1);

ℓ = the length of the node;

$l = H + 2\ell_{ex}$;

and

H = fuel height.

The weighted temperature coefficient, F_K, is

$$F_K = \left(\frac{\partial \rho}{\partial T}\right)_j (RW)_i. \qquad (3)$$

Finally, the temperature-induced reactivity feedback is given by

$$\sum_{K=1}^{NF} F_K \partial T_K = F_1 \partial T_1 + F_2 \partial T_2 + \ldots . F_{K-1} \partial T_{K-1} + F_K \partial T_K,$$

where the temperature in each radial and axial feedback node is multiplied by a radially and axially weighted temperature coefficient to compute the total reactivity feedback, $\rho(t)$. Thus, in the eight-channel dynamic-simulation model, we have 96 feedback networks that must be summed over to compute the total reactivity feedback associated with a rod-drop experiment.

The required input for the computations includes representative values for the effective delayed-neutron constants, averaged core and blanket temperature coefficients, and the averaged power and flow rate in each feedback channel. These data have led to very good agreement with zero-power transfer-function measurements. The effective delayed-neutron constants used to simulate the reactor kinetics are shown in Table I.

TABLE I. Effective Delayed-neutron Constants

Group	β_i	λ_i (sec)	Group	β_i	λ_i (sec)
1	0.000252	0.0127	5	0.001024	1.4000
2	0.001480	0.0317	6	0.000237	3.7800
3	0.001344	0.1150	β_{eff} = 0.007278		
4	0.002941	0.3110	ℓ_p^* = 1.55 x 10^{-7} sec		

*ℓ = Prompt-neutron lifetime.

For each type of core studied, "core-averaged" temperature coefficients of reactivity were computed for driver fuel, blanket material, and sodium coolant. These temperature coefficients[4] were obtained from a two-dimensional, six-group diffusion-theory digital program, and are listed in Table II. The core- and blanket-averaged temperature coefficients were distributed over each of the eight channels in our model, using the normalized reactivity-worth distributions shown in Figs. 3 and 4. These distributions were normalized to earlier ZPR-3

TABLE II. Core- and Blanket-averaged Temperature Coefficients of Reactivity for Stainless Steel-reflected and Depleted-uranium-blanketed Cores

Component	Depleted-uranium Radial Reflector; Stainless Steel Axial Reflector[a] (430 lh = 1% Δk/k) Temperature Coefficient (lh/°C)	Stainless Steel Radial Reflector; Stainless Steel Axial Reflector[b] (404 lh = 1% Δk/k) Temperature Coefficient (lh/°C)
Core sodium density	0.384	0.361
Density of sodium in radial blanket	0.066	0.099
Density of sodium in axial blanket	0.192	0.186
Axial expansion of fuel	0.213	0.183
Density of axial-blanket uranium[c] and stainless steel	0.079	0.080
Density of radial-blanket uranium and stainless steel	0.060	0.121

[a]Runs 29C, 33A, and 36A.
[b]Runs 26B and 29A.
[c]A small amount of depleted uranium not yet replaced by stainless steel.

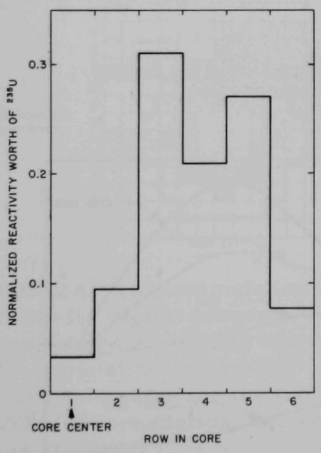

Fig. 3. Normalized Reactivity Worth of ^{235}U as a Function of Radial Position in the EBR-II Critical Mockup (adjusted for a typical EBR-II loading of driver-fuel and experimental subassemblies)

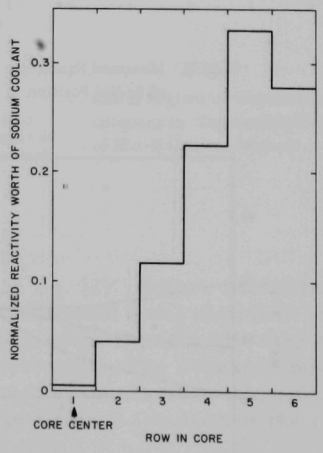

Fig. 4. Normalized Reactivity Worth of Sodium Coolant as a Function of Radial Position in the EBR-II Critical Mockup

critical-assembly mockups[5] of the original EBR-II core, and adjusted for a typical, current core loading that included experimental subassemblies. Additional critical experiments for present core loadings should appreciably improve this input data and will be utilized in future analysis of rod-drop experiments.

The measured reactivity worths of sodium in the EBR-II critical mockup in the radial and axial directions are depicted in Figs. 5 and 6. The mockup-core compositions are listed in Table III, and the inner and outer radii of the radial substitution regions are listed in Table IV and shown in Fig. 7. The weighted temperature coefficients were used in the radial direction as indicated by the normalized critical-assembly data, and the axial importance distribution was taken to be the square of a sine distribution integrated over the length of the individual fuel channel as available

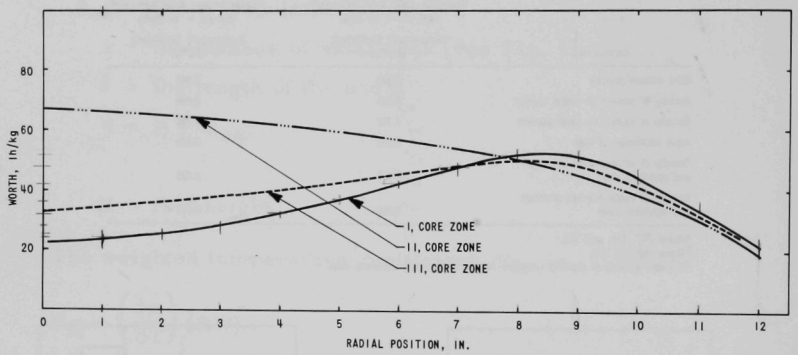

Fig. 5. Measured Reactivity Worths of Sodium Samples as a Function of Radial Position in the EBR-II Critical Mockup

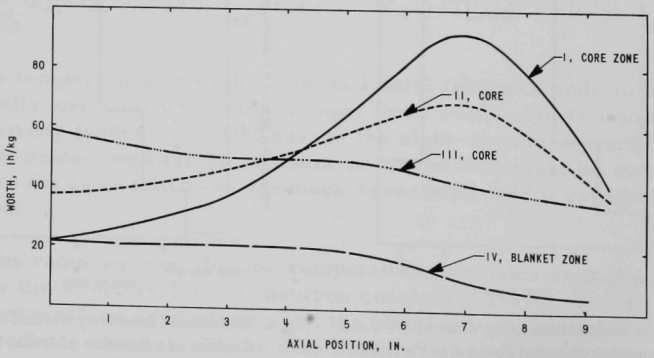

Fig. 6. Measured Reactivity Worths of Sodium Samples as a Function of Axial Position in the EBR-II Critical Mockup

TABLE III. Compositions of EBR-II Critical Mockup

	Sodium-filled Clean Core	Aluminum-filled Clean Core	Aluminum-filled Engineering Core
Critical Mass, kg ^{235}U:	161.6	161.0	166.2
	Composition (vol %)		
^{235}U (18.75 g/cc)	13.92	13.92	See
^{238}U (19.0 g/cc)	15.83	15.83	Table VIII
SS (7.85 g/cc)	16.86	19.31	of
Al (2.70 g/cc)		17.77	Ref. 5
Na (0.97 g/cc)	39.94		

TABLE IV. Inner and Outer Radii (in.) of Substitution Regions

Region	Sodium-filled Clean Core and Aluminum-filled Clean Core	Aluminum-filled Engineering Core
I	0-3.69	0-3.69
II	3.69-6.62	3.69-6.62
III	6.62-9.39	6.62-9.70
IV	10.21-12.69	9.70-15.50

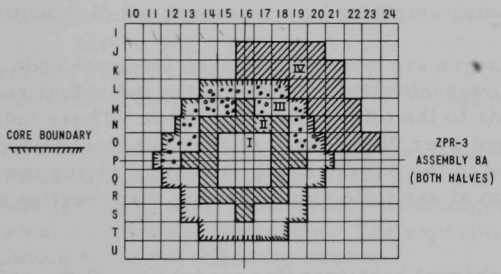

Fig. 7
Radial Regions of Material Substitutions in "Engineering Core" of EBR-II Critical Mockup

in AIROS-IIA. This formulation is given in Eq. (2). Future modifications to the AIROS-IIA digital program will allow additional axial distributions for the temperature coefficient of each feedback node, thereby allowing a closer dynamic simulation of the EBR-II characteristics. The averaged power levels and flow rates for the fuel and blanket channels were taken from the COOLTEMP[6] formulation, and are listed in Table V for each of the core loadings studied.

TABLE V. Averaged Power Levels and Flow Rates for Fuel and Blanket Channels

Channel Number	Simulation	Total Power = 41.5 MW Run 26B[a] Power (Btu/sec)	Flow (lb/sec)	Total Power = 45.0 MW Run 29A[a] Power (Btu/sec)	Flow (lb/sec)	Total Power = 45.0 MW Run 29C[b] Power (Btu/sec)	Flow (lb/sec)	Total Power = 50.0 MW Run 33A[b] Power (Btu/sec)	Flow (lb/sec)	Total Power = 50.0 MW Run 36A[b] Power (Btu/sec)	Flow (lb/sec)
1	Averaged Fuel Element (Row 1)	6.69	0.197	7.66	0.186	7.05	0.187	8.13	0.195	8.01	0.200
2	Averaged Fuel Element (Row 2)	7.22	0.197	7.61	0.186	7.95	0.187	8.02	0.102	7.90	0.108
3	Averaged Fuel Element (Row 3)	6.53	0.173	6.84	0.169	6.30	0.156	7.25	0.161	7.29	0.146
4	Averaged Fuel Element (Row 4)	6.27	0.127	6.43	0.131	6.23	0.127	7.48	0.126	7.35	0.129
5	Averaged Fuel Element (Row 5)	5.67	0.108	6.03	0.111	5.55	0.103	6.36	0.105	6.32	0.109
6	Averaged Fuel Element in Control Rods (Row 5)	5.63	0.126	6.01	0.129	5.54	0.119	6.27	0.124	6.24	0.126
7	Averaged Fuel Element (Row 6)	4.88	0.093	5.31	0.096	4.85	0.089	5.24	0.092	5.19	0.094
8	Averaged Blanket Element (Row 7)	0.64	0.042	0.66	0.043	5.95	0.127	4.80	0.135	5.26	0.136

[a]Stainless steel radial-blanket subassemblies.
[b]Depleted-uranium radial-blanket subassemblies.

In summary, the dynamic simulation of the EBR-II core is accomplished by using (a) eight channels of fuel and blanket elements, with radial weighting of reactivity worths in accord with a normalized distribution from the EBR-II critical mockup in ZPR-3, and (b) calculated temperature coefficients with axial weighting by a sine-squared distribution.

The temperature changes are computed in each feedback node and associated with a temperature coefficient to compute the individual reactivity contribution of the node to the total system feedback. These individual contributions are summed over 96 feedback nodes, and closed-loop feedback paths are computed in the AIROS-IIA formulation, giving the total reactivity of the system at any time step following the insertion of the stainless steel drop rod.

Implicit in the fuel-channel heat-transfer model are all the principal properties of uranium-5 wt % fissium driver fuel, stainless steel cladding, and sodium coolant. The AIROS-IIA dynamic simulation of EBR-II is as complete a model as we can presently utilize with existing digital programs. The accuracy and sensitivity of this model are discussed in the subsequent sections.

III. PHYSICAL CHARACTERISTICS OF EXPERIMENTAL CORE LOADINGS

Experimental rod-drop data from five different core loadings are analyzed in the following sections. These core loadings are shown in Figs. 8 through 12. The figures indicate the location of experimental subassemblies, driver-fuel subassemblies, safety and control rods, and the stainless steel drop rod. The environment surrounding the drop rod is worth noting, since this environment appreciably affects the at-power reactivity worth of the drop rod and the uncertainty associated with this reactivity worth.

Table VI gives the measured zero-power reactivity worths of the stainless steel drop rod in the core loadings studied. Two basic uncertainties are included in this table: (a) the reproducibility of the rod-drop worth at 500 kW, and (b) an estimate of the uncertainty in rod worth at full power due to increased neutron leakage from the reactor at full-power temperatures.

Characteristics of the experimental subassemblies are given in Appendix F. Figure 13 is a cross section of the EBR-II reactor showing the major components in the reactor vessel. Figure 14 is a schematic view of the reactor vessel and neutron shield assembly.

As noted in Table V, six averaged driver-fuel elements are simulated in our feedback model. Figure 15 is a pictorial view of the two types of EBR-II driver-fuel elements and subassemblies that were in the EBR-II core from runs 26B to 36B. Figures 16 and 17 show the physical design of the control and safety rods in the EBR-II core. Figure 18 shows the physical arrangement of fuel elements in the inner-blanket subassembly.

Averaged fuel elements from these subassemblies, representing individual radial-row locations in the core and blanket, were simulated to compute the temperature and reactivity changes associated with the stainless steel rod-drop experiments. The experimental and theoretical results are compared in the following section.

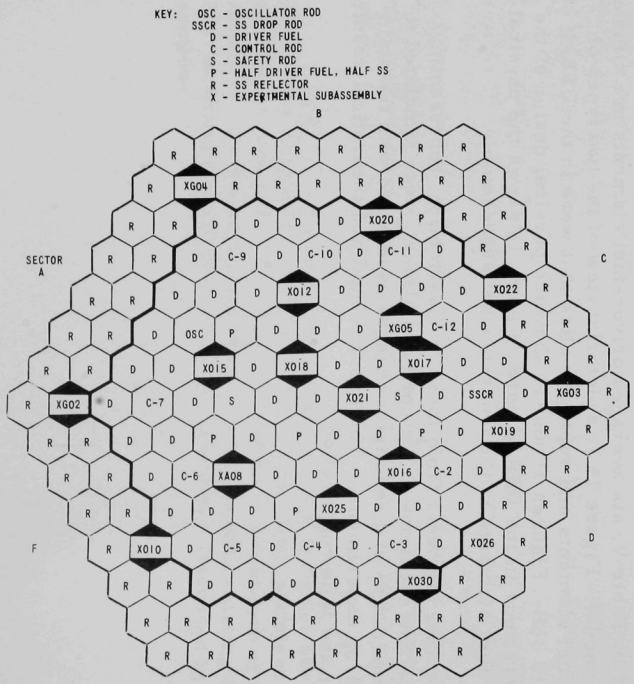

Fig. 8. EBR-II Loading Pattern, Run 26B

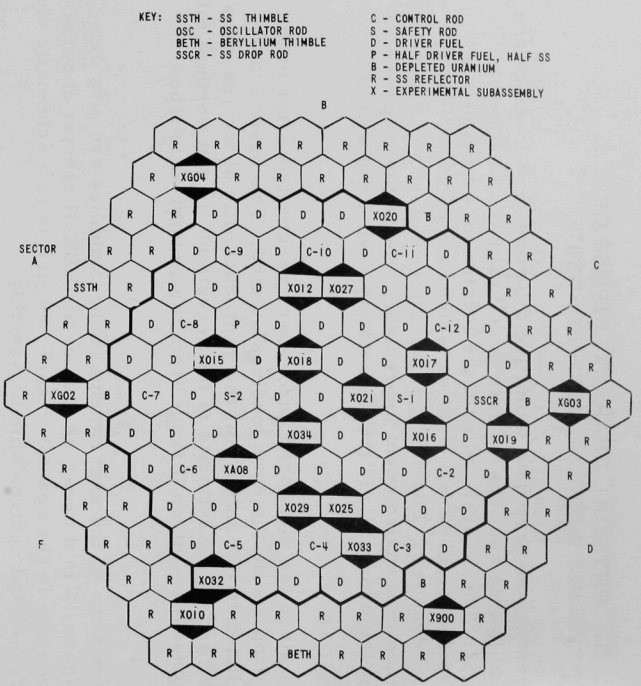

Fig. 9. EBR-II Loading Pattern, Run 29B

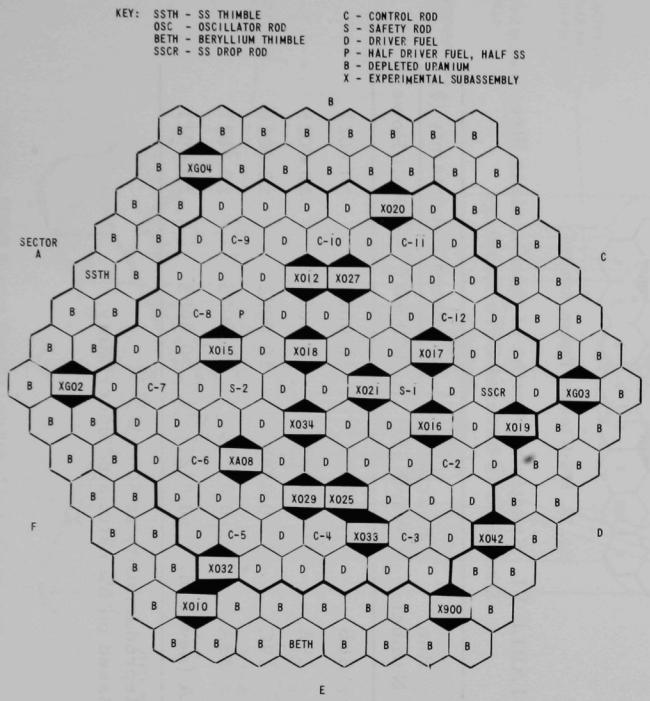

Fig. 10. EBR-II Loading Pattern, Run 29C

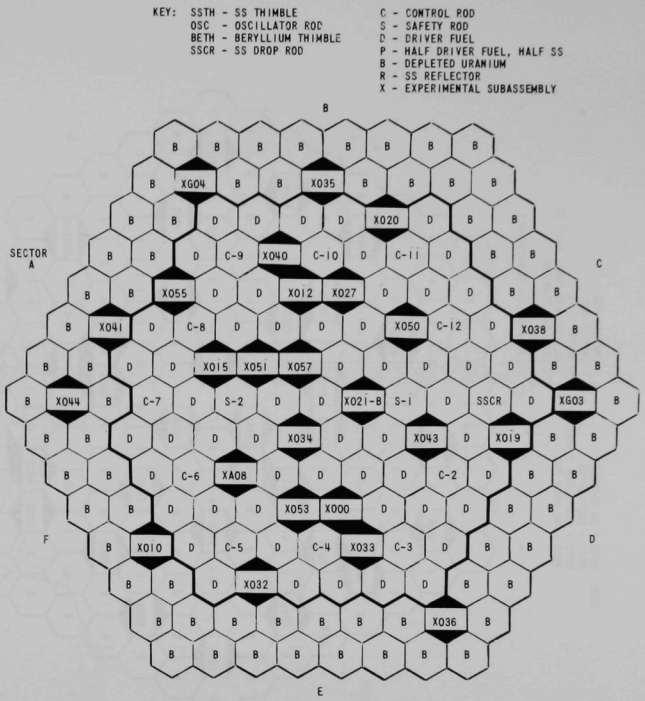

Fig. 11. EBR-II Loading Pattern, Run 33A

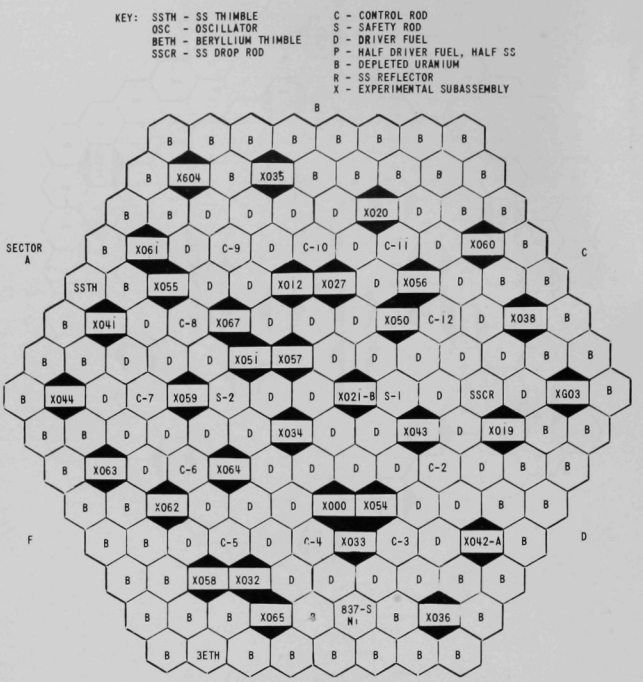

Fig. 12. EBR-II Loading Pattern, Run 36A

TABLE VI. Reactivity Worths of the Stainless Steel Drop Rod in Several Core Loadings

Run Number	Reactivity Worth ($)	Estimated Uncertainty ($)	
		At 500 kW[a]	At Full Power[b]
26B	0.0417	±0.0002	±0.0021
29A	0.0493	±0.0002	±0.0025
29C	0.0408	±0.0002	±0.0020
33A	0.0533	±0.0005	±0.0027
36A (new rod)	(0.0221)	±0.0005	±0.0011

[a]Reproducibility at 500 kW.
[b]Based on 5% estimated uncertainty.

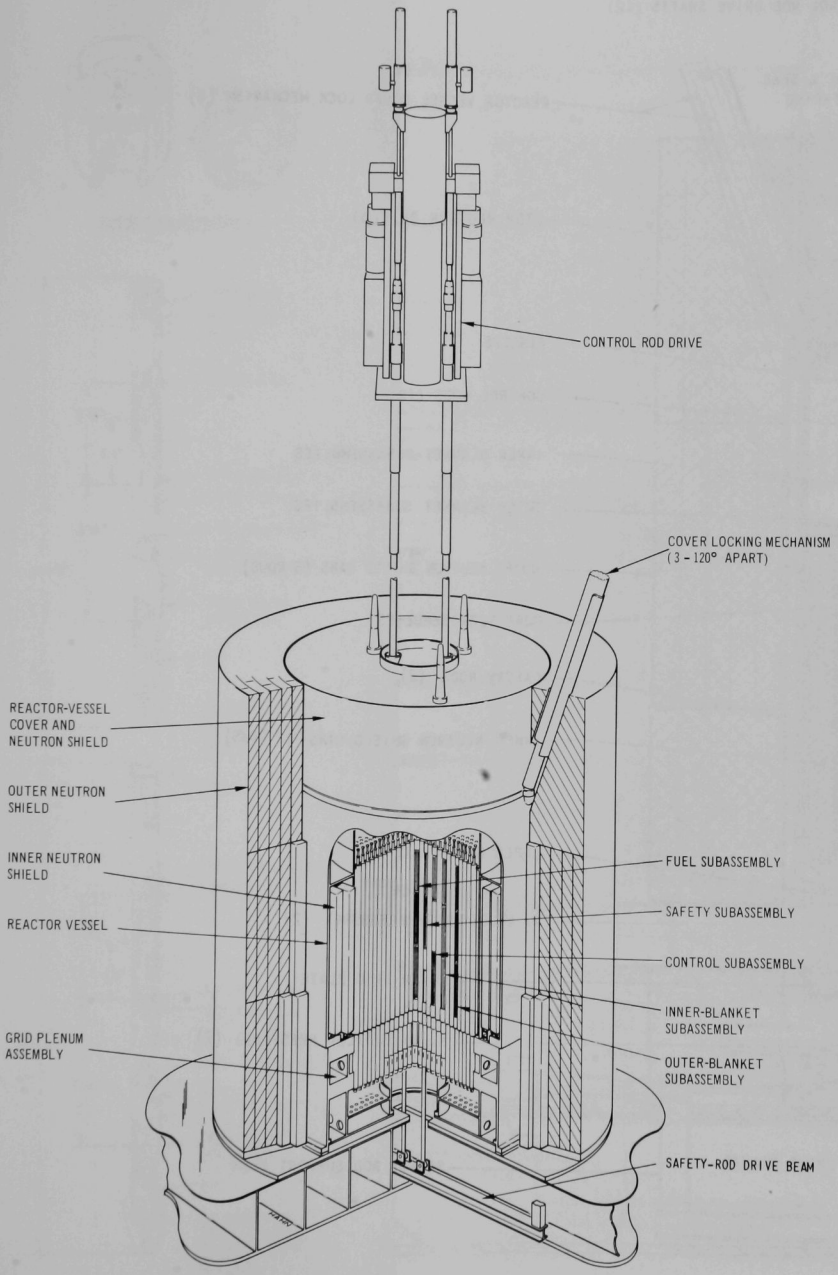

Fig. 13. EBR-II Reactor Showing Location of Major Components

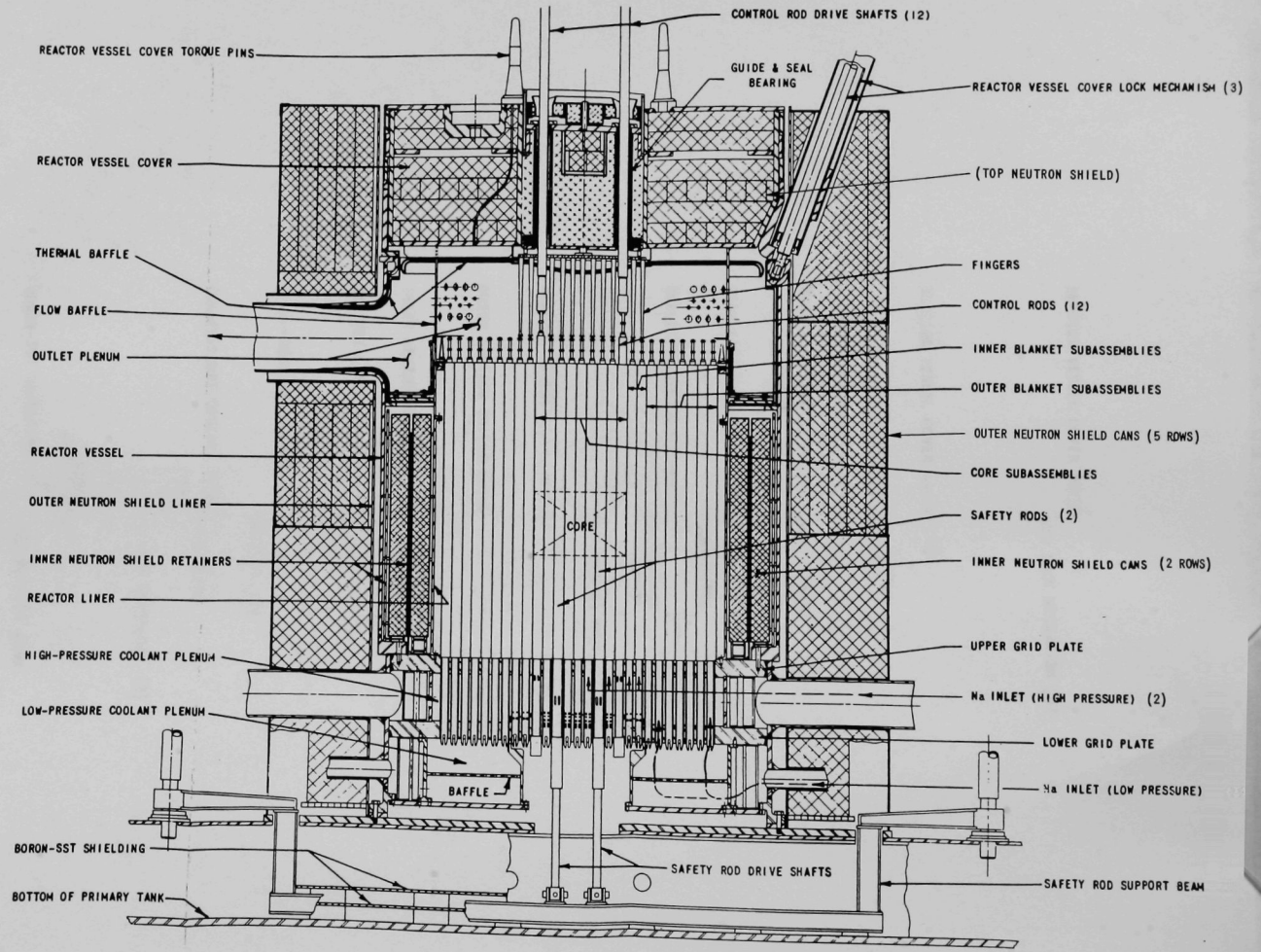

Fig. 14. Reactor Vessel and Neutron Shield Assembly

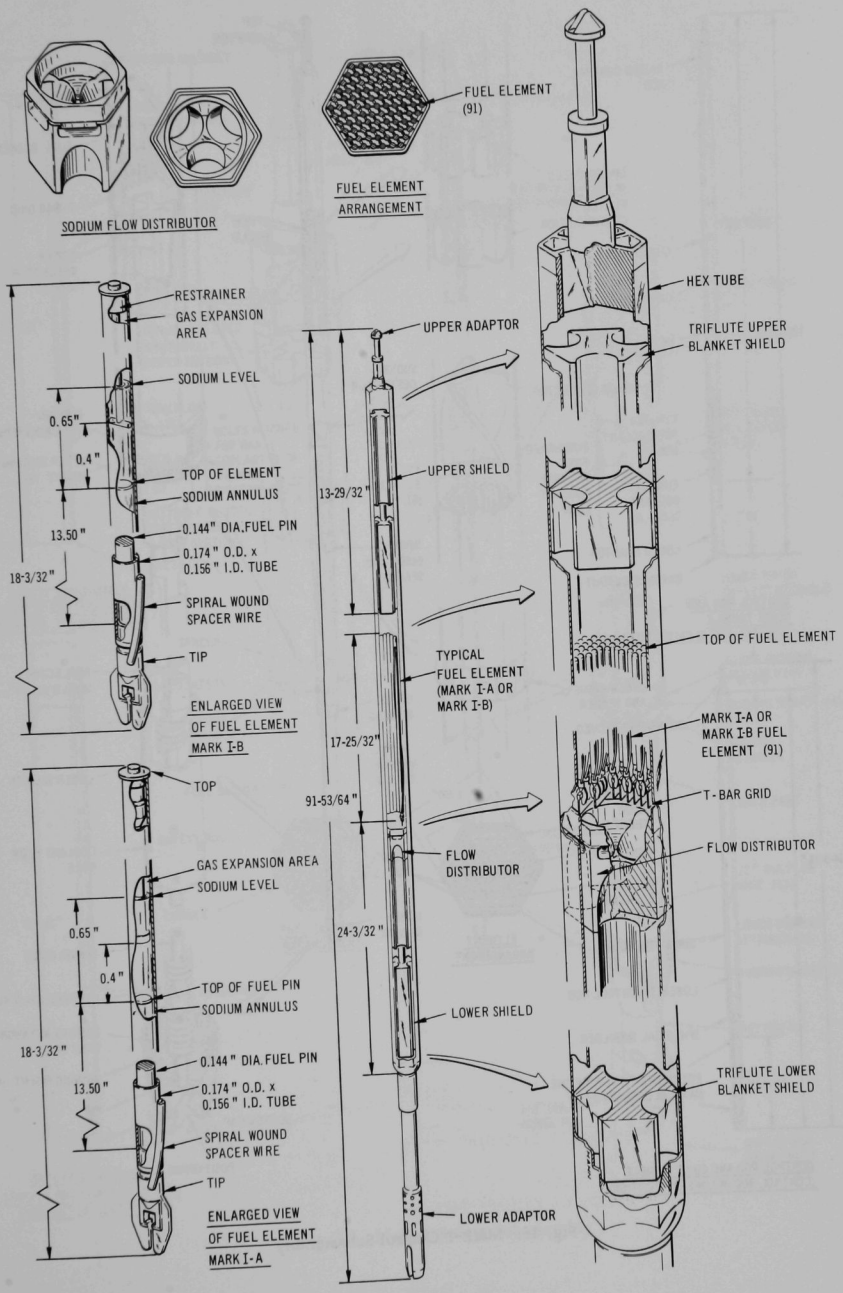

Fig. 15. Mark-IA and -IB Model STB Fuel Subassemblies

Fig. 14. Reactor Vessel and Neutron Shield Assembly

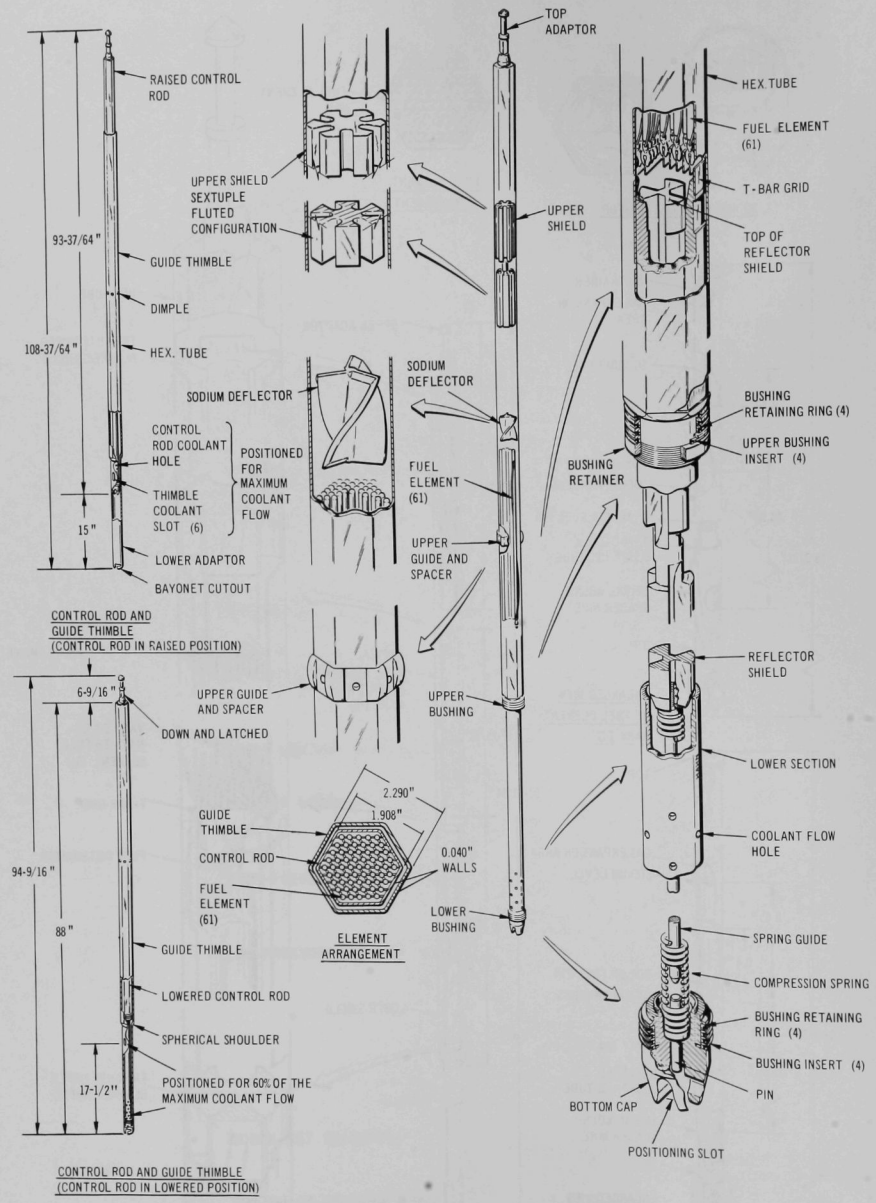

Fig. 16. Mark-I Control Subassembly

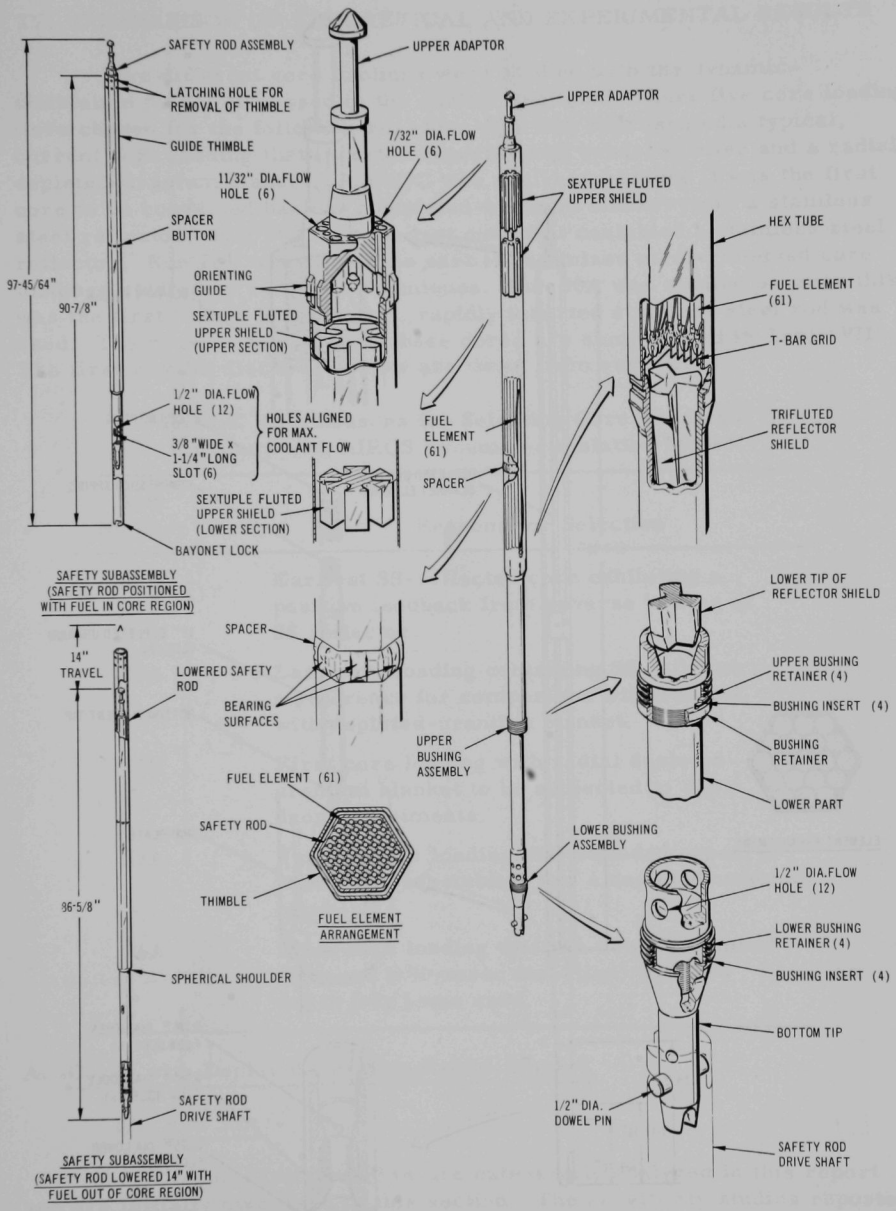

Fig. 17. Mark-I Safety Subassembly

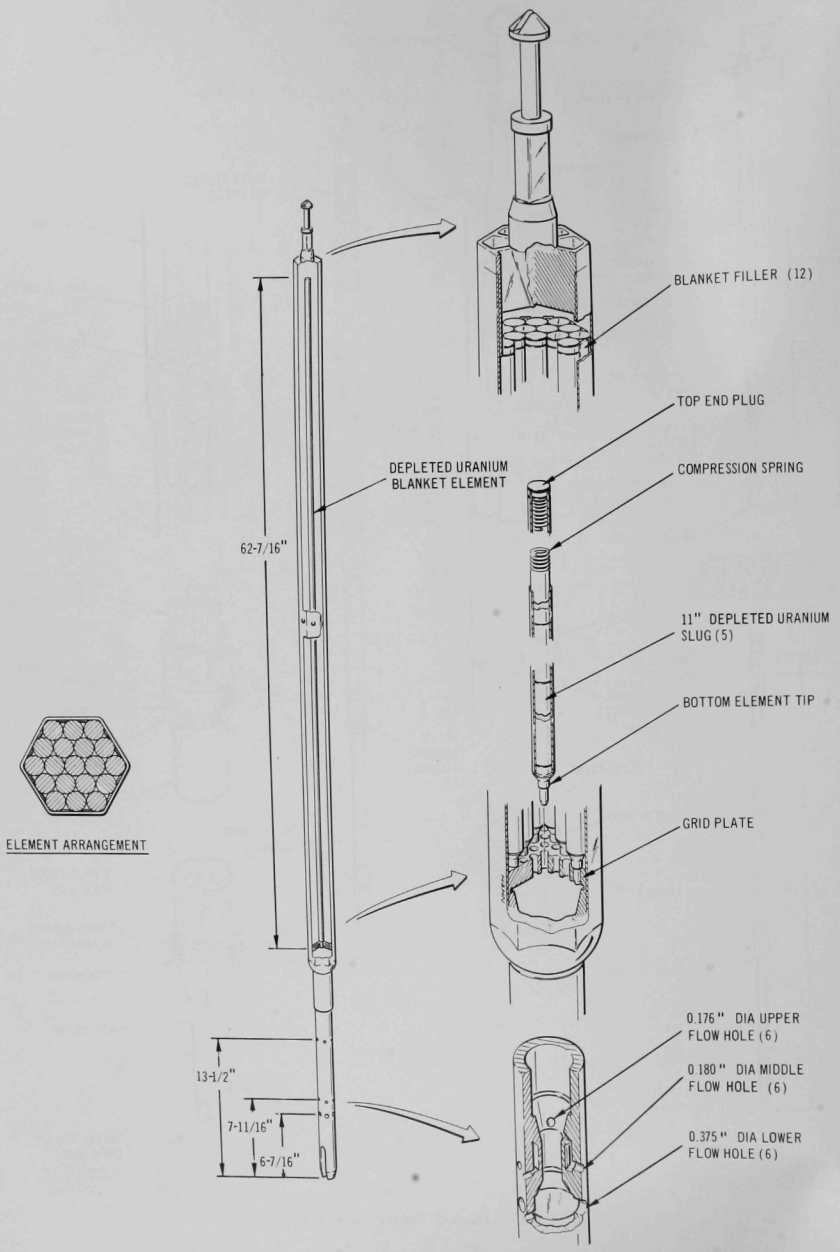

Fig. 18. Inner-blanket Subassembly

IV. COMPARISON OF THEORETICAL AND EXPERIMENTAL RESULTS

Five different core loadings were studied with the dynamic-simulation model discussed in the earlier sections. These five core loadings were chosen for the following reasons: Run 33A represented a typical, current core loading that included experimental subassemblies and a radial depleted-uranium blanket. Run 29C was analyzed because it was the first core to be converted back to a depleted-uranium blanket from a stainless steel reflector. Run 29A was the last core that contained a stainless steel reflector. Run 26B was one of the earliest stainless steel-reflected core loadings studied by rod-drop techniques. Run 36A was studied because this was the first time a lower-worth, rapidly inserted stainless steel rod was used. The reasons for study of these cores are summarized in Table VII. The first results discussed below are those from run 33A.

TABLE VII. Reasons for Selecting Core Loadings for Study with AIROS Dynamic-simulation Model

Run Number	Reasons for Selection
26B	Earliest SS-reflected core exhibiting a positive feedback from reverse bowing of SS reflector.
29A	Last core loading containing SS reflector; a reference for comparison with run 29C with depleted-uranium blanket.
29C	First core loading with radial depleted-uranium blanket to be subjected to rod-drop experiments.
33A	Typical core loading that included experimental subassemblies and a depleted-uranium blanket.
36A	First core loading where a new high-speed drop rod ($\approx$ 90-msec insertion) with low worth ($\approx 2\not{c}$) was used.

A. Cores with Depleted-uranium Radial Blanket

1. Run 33A

Results from run 33A are extensively analyzed in this report and are initially discussed in this section. The sensitivity studies reported in Sect. V deal solely with run 33A.

Figure 19 shows the experimental results obtained from the rod-drop experiment. The figure shows the computed reactivity feedback in dollars and the percentage of initial power level as functions of time. Also shown are the results obtained by using the dynamic model to simulate this experiment. Agreement is very good, and differences between measured and computed values are well within the experimental uncertainty inherent in the reduced experimental data (see Appendix A). These results indicate, as do other results given below, that the rod-drop experimental data essentially contain information relating to the feedback networks associated with driver-fuel axial expansion and sodium density changes, since these are the only effects that are computed in our initial dynamic-simulation model for EBR-II. Other delayed feedback terms can be identified in a theoretical feedback model (see Appendix E), but results for the first 40 sec of the rod drop indicate that they are not significant and need not be accounted for in the basic model. These results indicate, as do other comparisons given below, that the characteristics of the rod drop are reasonably well predicted, assuming that only fuel and coolant feedback networks for core and blanket are present for the first 40 sec following the drop. Additional feedback networks may be present but may be undetected because of uncertainties in experimental data (see Sect. V). Figure 20 shows results obtained at 27.5 MW and 100% flow for run 33A. The same excellent agreement is apparent.

To obtain an indication of the importance of the delayed-feedback terms, computed rod-drop results were compared with steady-state measurements of the EBR-II power coefficient. These steady-state

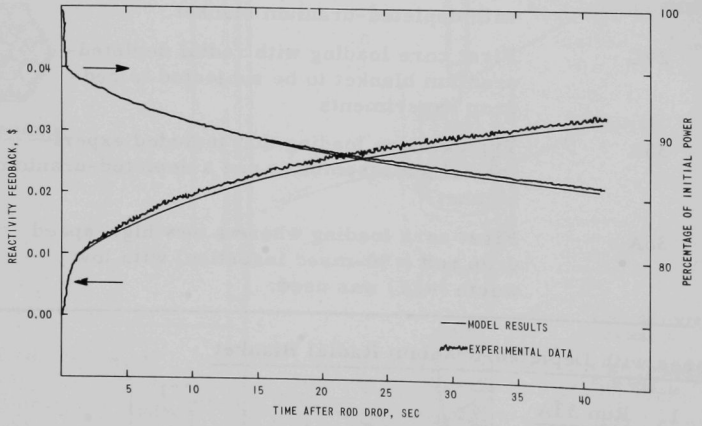

Fig. 19. Comparison of Model Results with Experimental Data for Run-33A Rod Drop (50 MW, 100% flow)

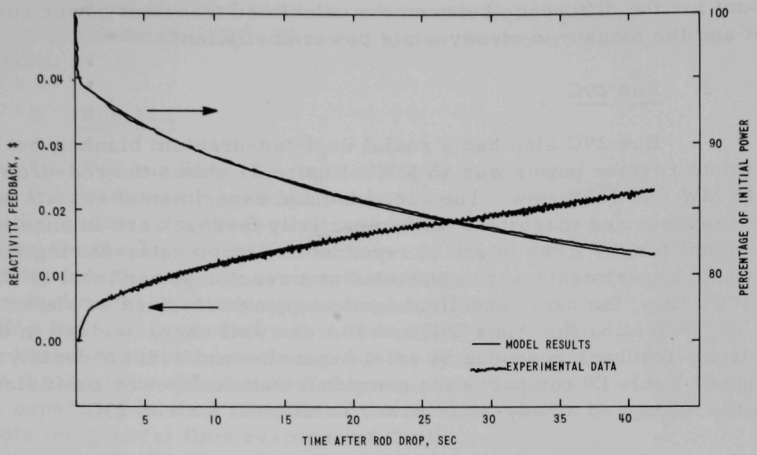

Fig. 20. Comparison of Model Results with Experimental Data for Run-33A Rod Drop (27.5 MW, 100% flow)

measurements are routinely made for each power run of EBR-II. They are made over the half-hour to hour following the initial change in power, and the associated change in reactivity is noted.

The steady-state measurements were compared with the transient power coefficient as obtained from computed rod-drop results at the end of 150 sec of computed feedback. Table VIII shows the results for run 33A.* The transient calculations yield a power coefficient of -1.25 Ih/MW, while the steady-state measurements yield values of -1.5 to -1.6 Ih/MW. Thus the calculated and experimental results differ by about 20%.

TABLE VIII. Computed Transient Power Coefficient Compared with Measured Steady-state Power Coefficient, Run 33A (No. 2 control rod inserted)

Initial Power Level (MW)	System Reactivity at 150 sec after Rod Drop (Ih)	Change in Reactor Power 150 sec after Rod Drop (MW)	Change in Reactivity 150 sec after Rod Drop (Ih)	Power Coefficient (Ih/MW)		% Difference Calc-Exp
				Transient Calculation	Steady-state Measurement	
50.0	-2.37	-11.31	+14.11	-1.25	-1.50 ± 0.10	-17%
27.5	-5.46	-8.82	+11.02	-1.25	-1.60 ± 0.10	-22%

We conclude from this comparison that the measurements of steady-state power coefficient imply additional delayed-feedback terms that are not contained in the 40 sec of recorded rod-drop experimental data. The delayed-feedback networks shown in Appendix E probably

*These results were obtained with the No. 2 control rod in the core. The rod-drop results of Figs. 19 and 20 were obtained with the No. 2 control rod removed so as to eliminate a possible shadowing effect on the stainless steel drop rod.

account for the difference between the calculated transient power coefficient and the measured steady-state power coefficient.

2. Run 29C

Run 29C also had a radial depleted-uranium blanket, but the maximum reactor power was 45 MW. Figure 21 shows the rod-drop results for 45 MW and 100% flow. The computed and experimental results for time response and magnitude of the reactivity feedback are in excellent agreement for the first 40 sec of recorded rod-drop data. During run 29C, additional experiments were conducted at a reactor power level of 22.5 MW and 100% flow; the same excellent agreement was obtained as shown in Fig. 22, indicating that runs 29C and 33A are well characterized in their reactivity-feedback response by axial expansion and sodium-density changes. Table IX compares the computed transient power coefficient with the measured steady-state power coefficient for run 29C.

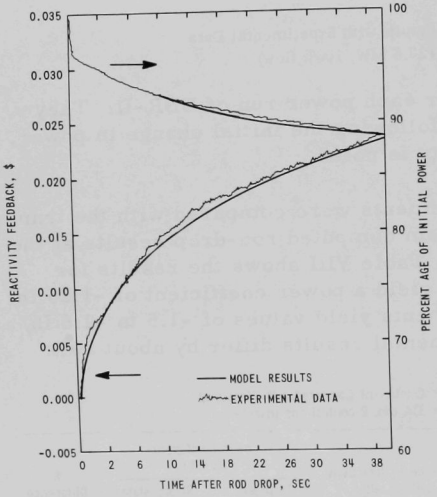

Fig. 21. Comparison of Model Results with Experimental Data for Run-29C Rod Drop (45 MW, 100% flow)

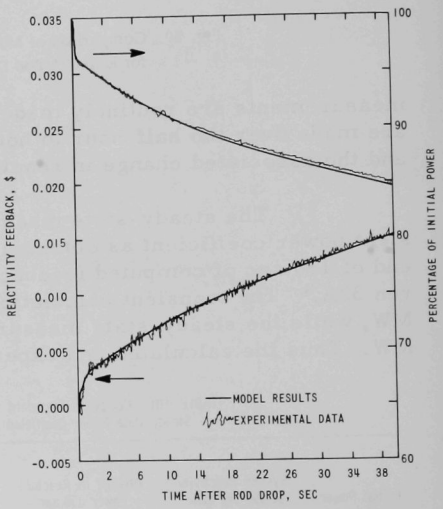

Fig. 22. Comparison of Model Results with Experimental Data for Run-29C Rod Drop (22.5 MW, 100% flow)

TABLE IX. Computed Transient Power Coefficient Compared with Measured Steady-state Power Coefficient, Run 29C

Initial Power Level (MW)	System Reactivity at 150 sec after Rod Drop (1h)	Change in Reactor Power 150 sec after Rod Drop (MW)	Change in Reactivity 150 sec after Rod Drop (1h)	Power Coefficient (1h/MW)		% Difference Calc-Exp
				Transient Calculation	Steady-state Measurement	
45.0	-1.968	-8.68	+10.70	-1.23	-1.70 ± 0.10	-28%
22.5	-4.82	-6.39	+7.85	-1.23	-1.70 ± 0.10	-28%

Runs 29C and 33A both used a stainless steel rod with a total worth of approximately 5¢. This rod had an effective insertion time of 280 msec.

3. Run 36A

For run 36A, the stainless steel drop rod was rebuilt to decrease the reactivity insertion time to 90 msec. However, the total worth of the drop rod was decreased to approximately 2¢. The reason for decreasing the insertion time of the drop rod was to introduce all of its reactivity into the reactor system in less time than the time constant of the driver-fuel metal, which is approximately 250 msec. The technique of dropping the stainless steel rod in less time than the driver fuel can respond to the initial power drop was used for the first time in run 36A; Fig. 23 shows the dynamic simulation of this run. A great deal of noise is indicated in the experimental data because of the low rod worth. However, the model predicts the general time response of the experimental data and is in very good agreement with the magnitude of the measured reactivity feedback.

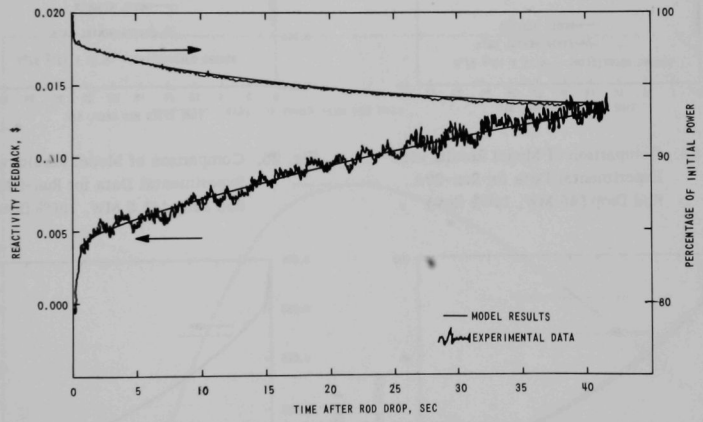

Fig. 23. Comparison of Model Results with Experimental Data for Run-36A Rod Drop (50 MW, 100% flow)

B. Cores with Stainless Steel Radial Reflectors

1. Run 29A

The basic dynamic-simulation model used in this report does not account for any reactivity feedbacks introduced from thermal bowing of core and blanket subassemblies resulting from temperature gradients in the core and blanket regions. Previous analysis[7] had shown that reverse bowing (inward toward the core) was present in the stainless steel blanket subassemblies durings runs 25 through 29A. Therefore, an attempt was made in the present study to fit the measured rod-drop data for run 29A,

assuming a variable positive bowing coefficient associated with sodium temperatures in the stainless steel reflector, along with constant temperature coefficients for fuel and coolant density changes as previously listed in Table II. Results of these fits are shown in Figs. 24 through 28. Figure 29 shows the positive blanket-subassembly-bowing coefficients required to fit the experimental data.

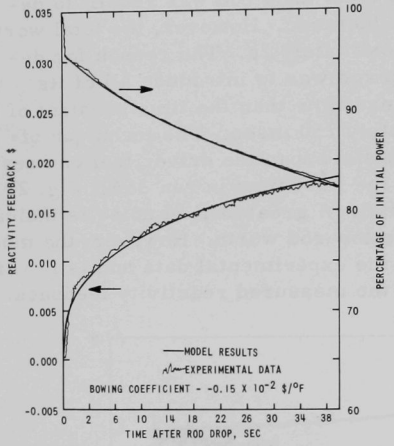

Fig. 24. Comparison of Model Results with Experimental Data for Run-29A Rod Drop (45 MW, 100% flow)

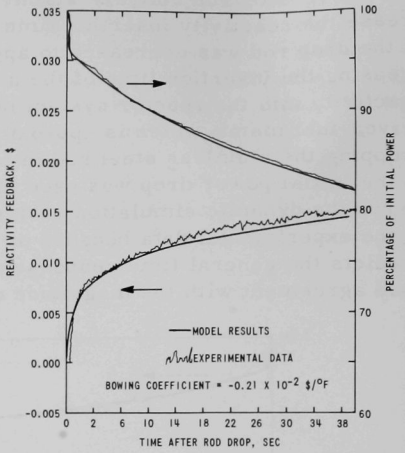

Fig. 25. Comparison of Model Results with Experimental Data for Run-29A Rod Drop (41.5 MW, 100% flow)

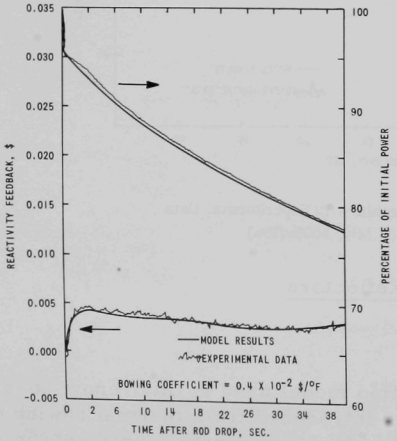

Fig. 26. Comparison of Model Results with Experimental Data for Run-29A Rod Drop (25 MW, 100% flow)

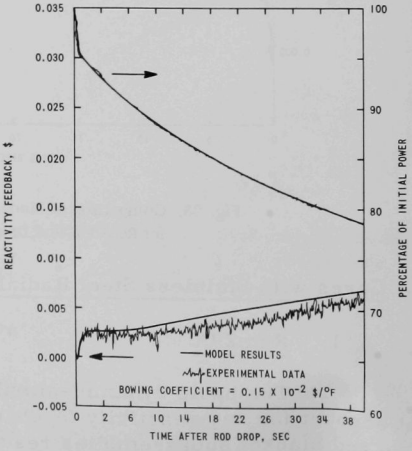

Fig. 27. Comparison of Model Results with Experimental Data for Run-29A Rod Drop (15 MW, 100% flow)

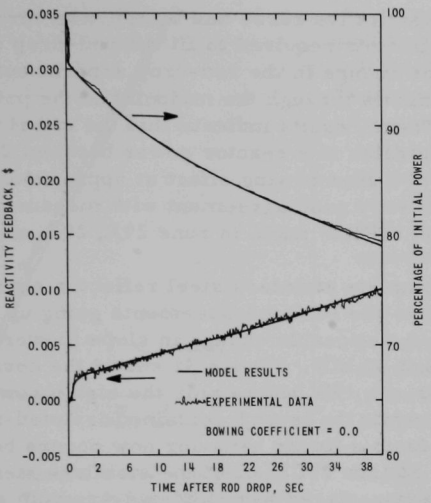

Fig. 28
Comparison of Model Results with Experimental Data for Run-29A Rod Drop (12.5 MW, 100% flow)

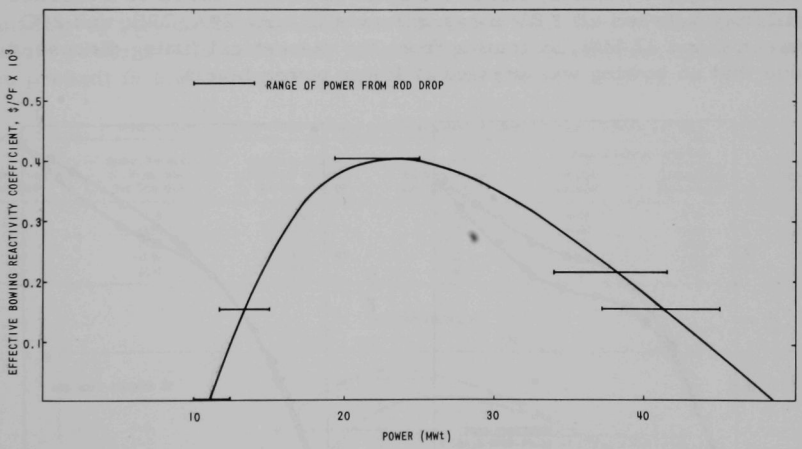

Fig. 29. Effective Bowing Reactivity Coefficient as a Function of Reactor Power for Run 29A

Of particular interest are the results of the rod-drop experiment in run 29A conducted at 12.5 MW and 100% flow. We observe here that the negative temperature coefficients listed earlier in Table II are sufficient by themselves to explain rod-drop data for the first 40 sec following the drop. The blanket-bowing coefficient here is equal to zero. This is an important result since it indicates that without the presence of subassembly bowing, the EBR-II core is well characterized by fuel axial expansion and sodium-density changes.

In Fig. 29, a semiquantitative curve has been drawn through the individual effective bowing coefficients required to fit the rod-drop data for run 29A. The range of power change in the rod-drop experiment is indicated. The curve has been drawn through the midpoint of the power range during the experiment. These results indicate that the effect of blanket-subassembly bowing saturates at a reactor power between 22 and 24 MW and that it extrapolates to a zero bowing effect at approximately 11 and 49 MW. This result is in very good agreement with measurements of the power-reactivity decrement (PRD) made in runs 29A, 29B, and 29C.

During run 29A a complete stainless steel reflector surrounded the EBR-II core. Figure 30 shows the PRD measurements going up and down in power, $0 \rightarrow 45 \rightarrow 0$ MW. A noticeable change in slope (power coefficient) occurs between 15 and 30 MW. Figure 31 shows the corresponding PRD measurements for run 29B, where only the eighth row contained stainless steel reflector, while the seventh contained depleted-uranium subassemblies. The departure from a linear behavior now occurs between 20 and 35 MW. Finally, in Fig. 32 (run 29C), all of the stainless steel reflector subassemblies have been replaced with depleted-uranium subassemblies, and a nearly linear behavior is noted. There is a marked similarity between all PRD measurements in runs 29A, 29B, and 29C between 0 and 12 MW, indicating from the theoretical fitting discussed above that no bowing was present at lower power levels.

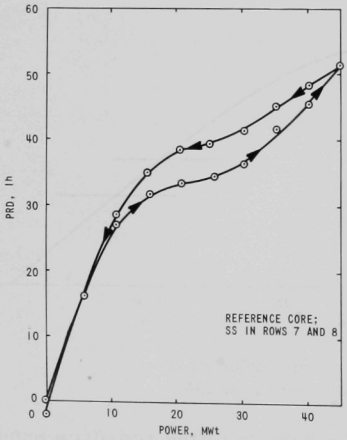

Fig. 30. Run-29A Power-coefficient Data, Normalized to a Rod Bank of 11.00 in.

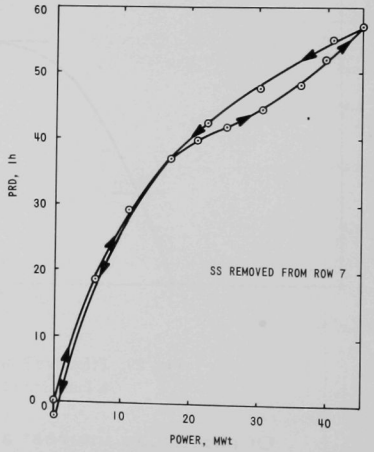

Fig. 31. Run-29B Power-coefficient Data, Normalized to a Rod Bank of 11.00 in.

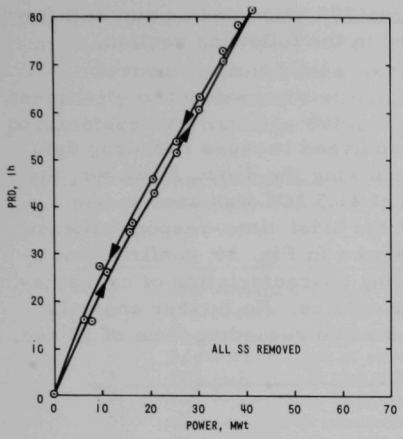

Fig. 32. Run-29C Power-coefficient Data Taken on July 16, 1968, Normalized to a Rod Bank of 11.00 in.

Table X compares the computed transient power coefficient with the measured steady-state power coefficient for run 29A. As shown, a considerable amount of reactivity is still in the system at the end of 150 sec in the transient calculation. The calculated power coefficients range from 10% higher to 50% lower than the corresponding measured power coefficients.

These results are shown semi-quantitatively in Fig. 33. The power coefficient is less negative as power is increased to approximately 20 to 24 MW, the points at which the dynamic model and the experimental results, respectively, indicate that the coefficient reaches its smallest negative value. Since these results are only semi-quantitative, they do not preclude that during a reactor transient at intermediate power levels, a zero or slightly positive coefficient could have been present in the vincinity of 22 MW in run 29A.

TABLE X. Computed Transient Power Coefficient Compared with Measured Steady-state Power Coefficient, Run 29A

Initial Power Level (MW)	System Reactivity at 150 sec after Rod Drop (Ih)	Change in Reactor Power 150 sec after Rod Drop (MW)	Change in Reactivity 150 sec after Rod Drop (Ih)	Power Coefficient (Ih/MW)		% Difference Calc-Exp
				Transient Calculation	Steady-state Measurement	
45.0	-7.35	-13.66	+10.33	-0.756	-0.732	+10.32
41.5	-8.90	-14.11	+8.78	-0.622	-0.567	+10.97
25.0	-15.53	-11.48	+2.15	-0.188	-0.522	-36.01
15.0	-12.87	-6.28	+4.81	-0.766	-1.910	-40.10
12.5	-12.03	-5.06	+5.65	-1.12	-2.170	-51.61

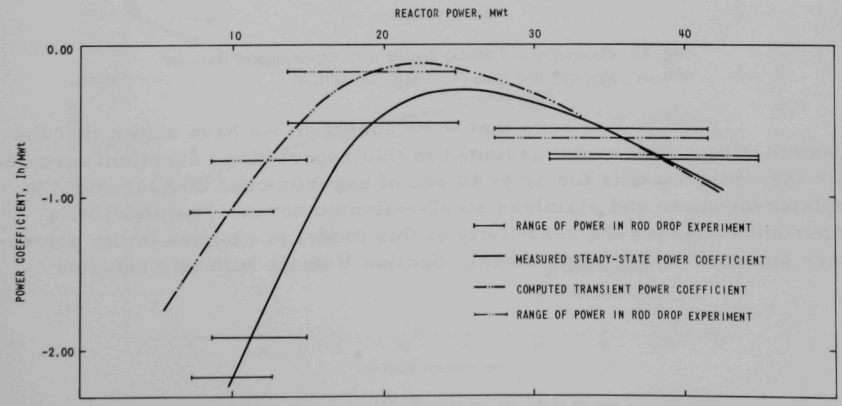

Fig. 33. Comparison between Computed Transient Power Coefficient (150 sec after rod drop) and Measured Steady-state Power Coefficient, in Run 29A

The dynamic model fitted to run 29A was used on run 26B for comparison, and the results are presented in the following section.

2. Run 26B

Run 26B was not extensively analyzed because rod-drop data were available for only the first 10 sec following the drop. However, the bowing coefficient obtained from run 29A at 41.5 MW was used to see whether the dynamic model would predict the brief time-response measurement made in run 26B. The results, shown in Fig. 34, confirm that a consistency does exist in the positive bowing characteristics of cores reflected with stainless steel blanket subassemblies. No further analysis was made of run-26B data because of the limited recording time of 10 sec.

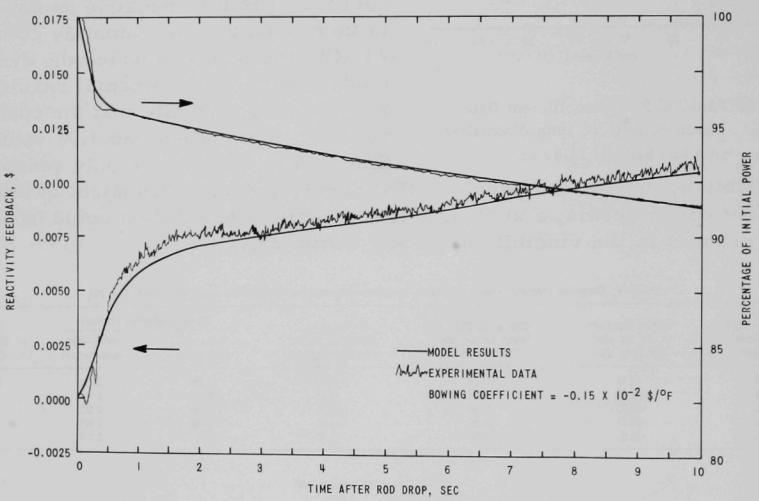

Fig. 34. Comparison of Model Results with Experimental Data for Run-26B Rod Drop (41.5 MW, 100% flow)

For the five runs that were analyzed, we have shown that the dynamic-simulation model assumed in this report gives excellent agreement with the rod-drop data for up to 40 sec of experimental measurement in depleted-uranium and stainless steel-reflected cores. However, it is important to assess the sensitivity of this model to changes in the parameters assumed in the basic model. Section V deals with this subject.

V. SENSITIVITY STUDIES

Several perturbations were made in the input parameters to test the sensitivity of the dynamic-simulation model to these parameters. The varied parameters are listed in Table XI.

TABLE XI. Parameters Varied in Sensitivity Studies of Run 33A[a]

Case No.	Type of Perturbation
1	10% reduction in core-sodium temperature coefficient
2	10% reduction in core-fuel temperature coefficient
3	Reduction to zero of core-sodium temperature coefficient
4	Reduction to zero of core-fuel temperature coefficient
5	10% reduction in radial-blanket-metal temperature coefficient
6	10% reduction in radial-blanket-sodium temperature coefficient
7	5% reduction in reactivity worth of stainless steel drop rod
8	5% increase in reactivity worth of stainless steel drop rod
9	Reduction to zero of radial-blanket-sodium temperature coefficient
10	Reduction to zero of radial-blanket-metal temperature coefficient
11	3% reduction in primary coolant flow
12	3% reduction in reactor power

[a]No. 2 control rod out of core.

The basis for comparison in these sensitivity studies was the rod-drop measurements made in run 33A with the No. 2 control rod out of the core. This run was chosen because of the good agreement between the "base-case" calculated results and the measured results. As Fig. 35 shows, the calculated curves fall right on top of the measured curves.

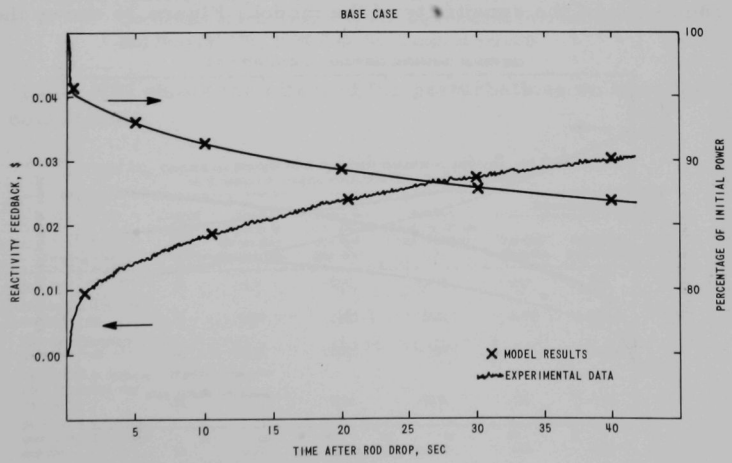

Fig. 35. Sensitivity-study Comparison of Model Results (Base Case) with Experimental Data for Run-33A Rod Drop (50 MW, 100% flow, No. 2 control rod out)

The sensitivity studies were conducted by varying the model parameters around the values shown in Table XII. The worth of the stainless steel drop rod was varied by ±5%, which is the assumed uncertainty in rod worth at full power; the primary-coolant flow and reactor power were reduced by 3%, which is the assumed uncertainty in these parameters.

TABLE XII. Sensitivity of Calculated Results to Changes in Input Parameters for the Dynamic-simulation Model (evaluated at 40 sec after rod drop)

Case No.	Type	$\frac{\partial \rho(\$)}{\partial X}$ [a]	$\frac{\partial P(\%)}{\partial X}$ [b]
1	∂X = 10% reduction in core-sodium temperature coefficient	-0.00069	-0.31
2	∂X = 10% reduction in core-fuel temperature coefficient	-0.00083	-0.34
3	∂X = Reduction to zero of core-sodium temperature coefficient	-0.00902	-3.36
4	∂X = Reduction to zero of core-fuel temperature coefficient	-0.01056	-3.96
5	∂X = 10% reduction in radial-blanket-metal temperature coefficient	-0.00003	-0.05
6	∂X = 10% reduction in radial-blanket-sodium temperature coefficient	-0.00005	-0.02
7	∂X = 5% reduction in reactivity worth of stainless steel drop rod	-0.00128	+0.64
8	∂X = 5% increase in reactivity worth of stainless steel drop rod	+0.00128	-0.64
9	∂X = Reduction to zero of radial-blanket-sodium temperature coefficient	-0.00042	-0.17
10	∂X = Reduction to zero of radial-blanket-metal temperature coefficient	-0.00063	-0.30
11	∂X = 3% reduction in primary coolant flow	+0.00039	+0.12
12	∂X = 3% reduction in reactor power	-0.00046	-0.22

[a] ρ = Reactivity.
[b] P = Power.

The results of many of the perturbations listed in Table XII were small and are not worth showing graphically. However, some were dramatically indicative of the sensitivity of the model. Figure 36 shows the

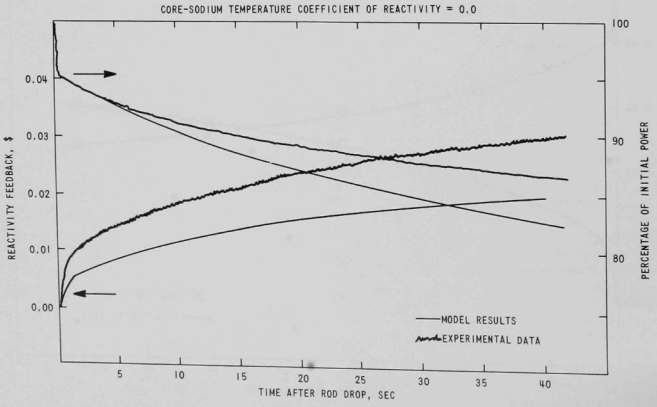

Fig. 36. Sensitivity-study Comparison of Model Results (Core-sodium Temperature Coefficient of Reactivity = 0) with Experimental Data for Run-33A Rod Drop (50 MW, 100% flow, No. 2 control rod out)

computed results assuming that there is no sodium-temperature-induced reactivity coefficient in the dynamic-simulation model. The computed results depart markedly from the experimental data, indicating that there is a definite feedback from the sodium coolant and that this feedback is included in the rod-drop experimental data. Figure 37 shows the result of assuming that the fuel-temperature-induced reactivity coefficient is equal to zero. Here again we note a marked departure from the experimental data, indicating that feedback from the fuel temperature is included in the rod-drop experimental data.

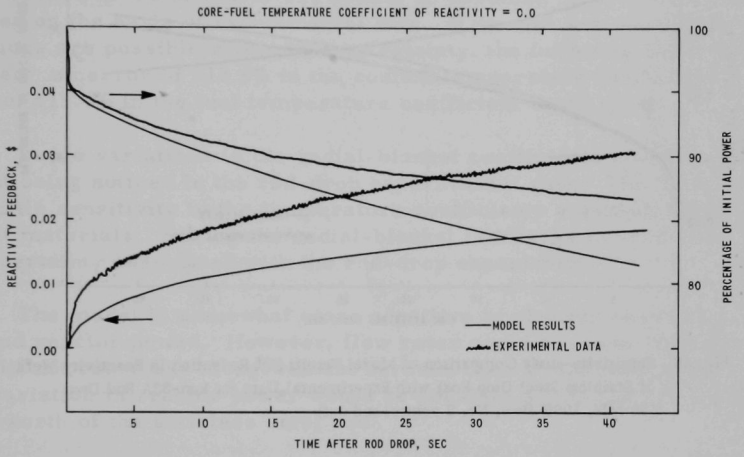

Fig. 37. Sensitivity-study Comparison of Model Results (Core-fuel Temperature Coefficient of Reactivity = 0) with Experimental Data for Run-33A Rod Drop (50 MW, 100% flow, No. 2 control rod out)

Table XIII shows the effect of the perturbations on computed transient power coefficients.

TABLE XIII. Computed and Measured Power Coefficients (transient vs steady-state) with Assumed Changes in Parameters in Feedback Model [Run 33A: No. 2 control rod out]

Parameter Change	Initial Power Level (MW)	System Reactivity at 150 sec after Rod Drop (1h)	Change in Power 150 sec after Rod Drop (MW)	Change in Reactivity 150 sec after Rod Drop (1h)	Power Coefficient (1h/MW)		
					Transient Calculation	Steady-state Measurement	% Difference Calc-Exp
Base Case	50	-2.17	-10.73	+13.38	-1.25	-1.50	-17.0
Core-sodium temperature coefficient = 0.0	50	-4.94	-15.15	+10.61	-0.700	-1.50	-54.0
Core-fuel temperature coefficient = 0.0	50	-5.56	-15.95	+ 9.99	-0.626	-1.50	-58.0
5% reduction in reactivity worth of stainless steel drop rod	50	-2.00	-10.23	+12.76	-1.25	-1.50	-17.0
5% increase in reactivity worth of stainless steel drop rod	50	-2.33	-11.22	+13.99	-1.25	-1.50	-17.0
3% reduction in total reactor coolant flow	50	-2.09	-10.56	+13.46	-1.27	-1.50	-15.0
3% reduction in total reactor power	48.5	-2.29	-10.63	+13.26	-1.25	-1.50	-17.0

The variation in worth of the stainless steel drop rod is extremely important, since this variation turns out to be the limiting factor in using the measured results as a basis for assessing changes in the model results. Figures 38 and 39 show that varying the rod worth by 5% causes an

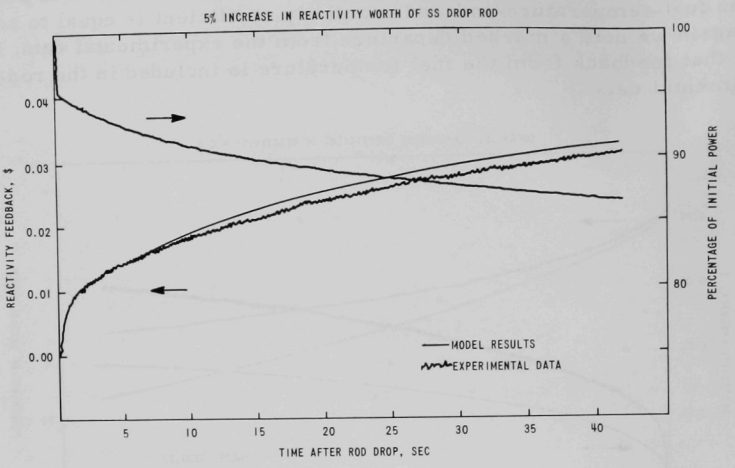

Fig. 38. Sensitivity-study Comparison of Model Results (5% Reduction in Reactivity Work of Stainless Steel Drop Rod) with Experimental Data for Run-33A Rod Drop (50 MW, 100% flow, No. 2 control rod out)

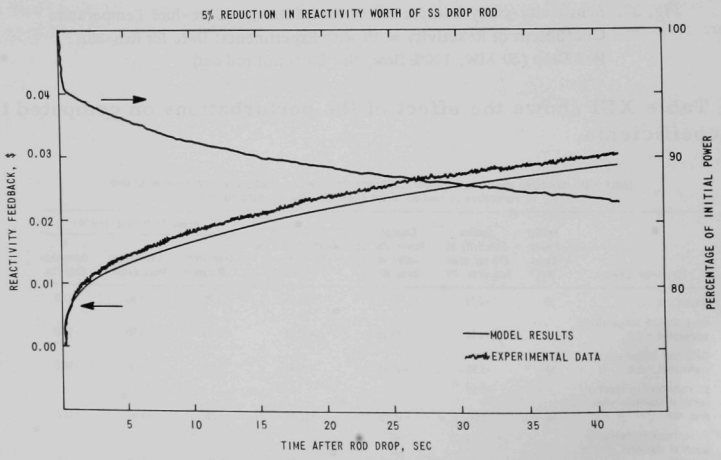

Fig. 39. Sensitivity-study Comparison of Model Results (5% Increase in Reactivity Work of Stainless Steel Drop Rod) with Experimental Data for Run-33A Rod Drop (50 MW, 100% flow, No. 2 control rod out)

appreciable departure from the experimental results based on the assumed (unperturbed) rod worth. As the values in Table XIII show, a variation of ±5% in rod worth causes a reactivity variation of ±0.00128$ at the end of 40 sec in the dynamic simulation. Thus, with a 5% assumed uncertainty in the worth of the stainless steel rod, any reactivity variations of less than 0.00128$ at the end of 40 sec of recorded rod-drop data are not statistically significant, since they lie inside the uncertainty of the experimental data.

This means that in judging the model results, any variations of less than 0.00128$ at the end of 40 sec cannot be assumed to be in error and adjusted on the basis of experimental data. If we now ask what kinds of variations are possible within this uncertainty, the following results are obtained: an error of ±18.6% in the sodium temperature coefficient or an error of ±15.4% in the fuel temperature coefficient could exist.

Large variations in the radial-blanket coefficients could be included without being noticed in the rod-drop experimental data. The model shows very little sensitivity to the temperature coefficients assumed for the radial-blanket materials. Setting the radial-blanket feedbacks to zero is well within the uncertainty associated with the rod-drop experiment.

The model is somewhat more sensitive to changes in primary coolant flow and reactor power. However, flow rates could be off by 9.8% or less and still not cause any disagreement between theory and experiment. An 8.3% variation in reactor power would be possible within the ±5% uncertainty in the worth of the stainless steel rod.

These sensitivity studies highlight the importance of knowing the worth of the drop rod accurately. The worth should be known to within 1% in order that the experimental data can be used to obtain good information on the temperature-induced reactivity-feedback networks associated with the transient behavior of EBR-II cores. This greater accuracy is especially required in assessing the control-rod "bank effect" (the differential expansion of control-rod drive shafts with respect to the EBR-II core). The control rod bank effect is probably undetected in present studies because of uncertainties attributed to the experimental data.

VI. SUMMARY AND CONCLUSIONS

The dynamic-simulation model used in this report couples the neutronic, thermal, and hydraulic characteristics of the EBR-II core into a closed-loop reactivity-feedback system for analysis of the experimental rod-drop data. With the use of only fuel axial-expansion effects and sodium-density effects, we are able to reproduce the rod-drop data qualitatively (as regards time response) and quantitatively (as regards magnitude of the reactivity feedback) over the first 40 sec of experimental recording time.

Through the assumption that one parameter is unknown (a variable positive bowing coefficient) and that there are constant negative computed feedbacks, we can show that rod-drop data acquired from stainless steel-reflected cores agree with this model. The semiquantitative results are in agreement with other types of measurements made during the time EBR-II was loaded with a stainless steel reflector.

The following conclusions of our studies can be listed:

1. The prompt feedback networks in EBR-II up through run 36A are principally composed of fuel axial-expansion effects and sodium-density effects.

2. Positive bowing from the stainless steel reflector was present in cores from runs 26B through 29A.

3. At low power levels (< 12.5 MW) with a stainless steel reflector there was no thermal bowing, and under those conditions, the basic dynamic model using only computed negative temperature coefficients gave excellent agreement with rod-drop data.

4. Assuming a $\pm 5\%$ uncertainty in the reactivity worth of the stainless steel drop rod, the following variations could be made in the system parameters while remaining inside the uncertainties of the experimental data:

   a. $\pm 18.6\%$ variation in the sodium temperature coefficient;

   b. $\pm 15.4\%$ variation in the fuel temperature coefficient;

   c. $\pm 9.8\%$ variation in the primary coolant flow;

   d. $\pm 8.3\%$ variation in the reactor power.

5. The reactivity feedbacks in the radial blanket can be assumed to be zero without significantly affecting the comparison of theoretical and experimental rod-drop data.

6. There definitely are reactivity feedbacks from sodium-coolant temperature changes and fuel-expansion effects in the rod-drop data, since zeroing out these effects causes the model to deviate markedly from the experimental data.

7. This dynamic-simulation model can be used toward analyzing the transient response of EBR-II cores containing irradiation experiments.

8. The agreement obtained with the dynamic model used justifies the assumption that the power coefficient is linear at reactor operating levels.

VII. RECOMMENDATIONS

The following recommendations are made as a result of comparing the dynamic-simulation model with experimental rod-drop data:

1. The drop rod should have at least 5¢ of reactivity worth to avoid signal-to-noise problems in data reduction.

2. The uncertainty in the reactivity worth of the drop rod should be no more than 1% to allow detailed interpretation of the various feedback networks in the EBR-II core.

3. An instrumented subassembly containing driver fuel can greatly enhance our interpretation of the rod-drop data. With fast-response thermocouples on the fuel, cladding, and coolant regions of this metallic driver-fuel subassembly, we can further verify that the temperature variations computed in the AIROS dynamic-simulation model are consistent with those measured; we can also compare computed reactor results with the ion-chamber current reflecting the power variation in the reactor following the rod drop.

4. Methods should be developed to eliminate noise from the output data associated with reactivity feedback.

5. A statistical analysis should be developed or adapted to identify clearly statistically significant variations in the measured feedback-reactivity data prior to detailed dynamic-simulation modeling of future rod-drop experiments.

ACKNOWLEDGMENTS

The author wishes to acknowledge the discussions with the guidance from R. R. Smith and W. B. Loewenstein, which led to the timely completion of this analytical study. In addition, the author wishes to acknowledge the technical assistance of I. A. Engen in providing the reduced experimental rod-drop data and in providing Appendix A of this report, which describes the methods used in reducing the experimental data.

APPENDIX A

Experimental Rod-drop Techniques and Uncertainties

A. Experimental Mechanism and Data-reduction Techniques for Rod-drop Experiments

Rod-drop experiments are conducted in EBR-II to evaluate reactivity feedback. A special stainless steel control rod is dropped out of the reactor core, causing a drop in reactor power. Drop-rod position, reactivity worth as a function of position, and reactor power are recorded and used as input to an inverse-kinetics computer code, which computes system reactivity and subtracts the reactivity change due to the dropped rod. The result is the reactivity feedback in the system during the experiment. The rod-worth calibration is determined as a function of rod position from experiments conducted at a reactor power level of 500 kW, where feedback effects are negligible. Typically, three to five rod-drop experiments are conducted for a given set of power and coolant-flow conditions, and the results are averaged.

Evaluation of the results requires consideration of the experimental mechanism, the data-acquisition system, and the data-reduction or computational techniques.

1. The Experimental Mechanism

The special stainless steel rod is installed in place of a standard control rod. The rod contains stainless steel instead of fuel pins, resulting in a reactivity worth for the rod of 0.04$ to 0.05$, compared to about 0.50$ for a standard control rod similarly situated.

Modification of the reactor control system allows the rod to be dropped independently of the remaining standard control rods. During an experiment a signal trips the latching mechanism, and the rod falls through a stroke of 14 in. in about 0.28 sec. The rod is decelerated through the last 6 in. of travel by a dashpot. Following each drop, the rod is raised back into the core and reactor power is leveled. Successive experiments require 15 to 20 min of separation to allow equilibrium delayed-critical conditions to be reestablished.

2. Data-acquisition System[2]

The data-acquisition system consists of a neutron detector, a rod-position indicator, electronic signal-conditioning and -transmission equipment, an analog-to-digital (A/D) converter, and an IBM-1620 computer.

a. Neutron Detector

The neutron detector is a General Electric Model NA09 compensated ion chamber, operated without the compensating voltage. The chamber is located in the J4 instrument thimble, which penetrates the neutron shield surrounding the reactor vessel. The detector location with respect to the core is shown in Fig. 40.

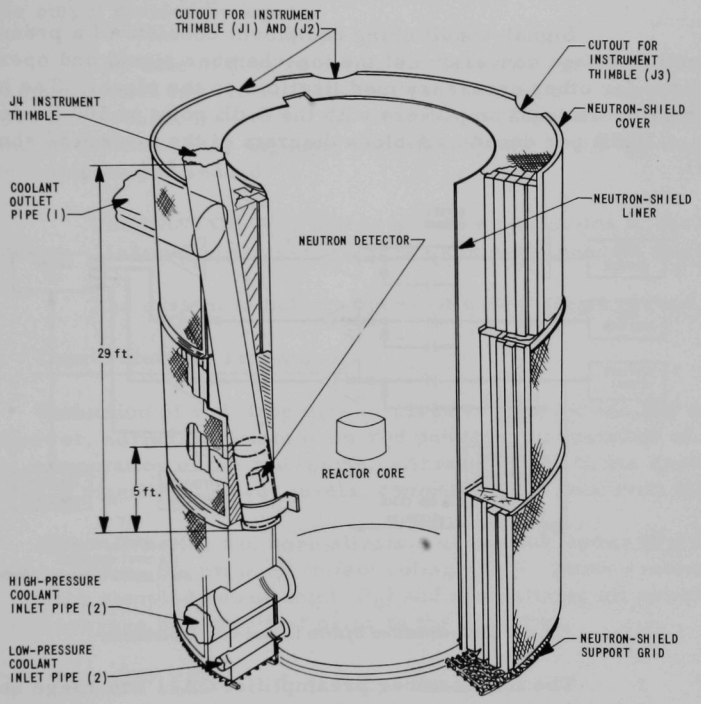

Fig. 40. Location of Neutron Detector

b. Rod-position Indicator

Rod position is obtained as a 0- to 10-V signal from a potentiometer connected to the stainless steel drop rod.

c. Electronics System

All data obtained from the sensors are in analog form, which must be converted to digital values for storage in the computer. Signals presented to the A/D converter must lie in the range of ±10 V,

and signal conditioning is performed to provide adequate signals. Rod-drop experiments present three input signals to the A/D converter: (a) ion-chamber output, (b) rod position, and (c) initiate signal. The initiate signal controls the acquisition of data by the computer and the release of the drop rod. Release of the rod occurs a specified time after the computer begins accumulating data. The time delay is controlled by a counter and allows collection of power data prior to the drop for normalization of power data acquired during the experiment.

Signal-conditioning equipment consists of a preamplifier for current-to-voltage conversion of the ion-chamber signal and operational amplifiers for other necessary modifications to the signal. The amplifiers are Nexus operational amplifiers with the 3-dB point at 500 Hz and an attenuation of 20 dB per decade. A block diagram of the system is shown in Fig. 41.

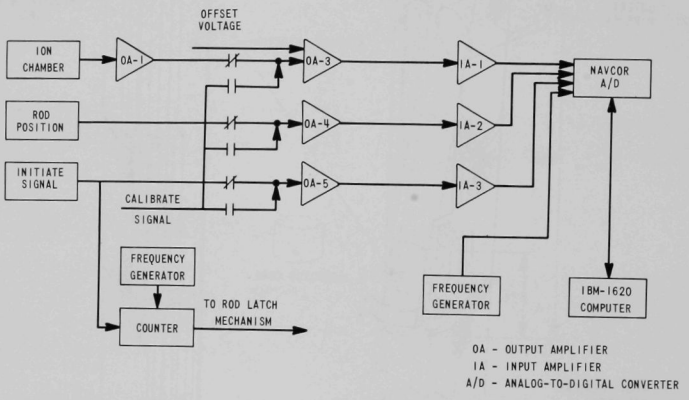

Fig. 41. Data-aquisition System for Rod-drop Experiments

The ion-chamber preamplifier OA-1 has range selection for maintaining the output signal in the range of 2 to 8 V. Operational amplifiers OA-3 through OA-5 have variable gain selection from 0.01 to 1000 scale units for signal modification. Attenuators IA-1 through IA-3, just before the A/D converter, are 10-turn potentiometers for further signal modification to maintain data within allowable limits at the digitizer. Output from the digitizer lies between -1.8 and +1.8 V, and consists of four significant digits. Digitizer output is stored by the computer and written on magnetic tape upon completion of data acquisition for an experiment.

In order to provide an adequate representation of reactor power, most of the constant component of power is subtracted from the ion-chamber signal by an offset voltage (OSV) at OA-3. The output of OA-3 then represents the changing component of reactor power during an experiment.

Reconstruction of the power signal for inverse-kinetics computation is accomplished by calibrating the system gain from OA-3 through the computer and adding the product; system gain times OSV, to each power-data point. This is done at the time of the inverse-kinetics computation, rather than at the time of data acquisition.

System calibration is accomplished by injecting a known voltage into OA-3 and averaging the output to the computer. The system gain equals output divided by input.

The rate of data sampling is controlled by a frequency generator and counter used as a clock. Data may be sampled at a rate up to about 300 samples per second, limited by the time required for the computer to connect and disconnect to the digitizer and store data. A typical sampling rate is 200 samples per second.

The NAVCOR A/D unit is a field modification to the IBM-1620 computer. Maximum time skew between sampled channels is 160 μsec.

The system is battery operated with a single ground.

3. Data-reduction Techniques

Reduction of rod-drop data involves reconstruction and normalization of power, normalization of drop-rod position, computation of system reactivity, computation of the rod-worth calibration, and, in the case of experiments at significant power levels, computation of reactivity feedback.

Reconstruction and normalization of reactor power (P_i) is accomplished by adding the product: offset voltage (OSV) times system gain (G), to each sampled power point (P_s) and normalizing all power data to a 24-point average of power just prior to the rod drop:

$$P_i = P_s + OSV \times G; \quad i = 1, 2, \ldots, N;$$

$$P_0 = \frac{1}{24} \sum_{i=1}^{24} P_i;$$

$$P_i = P_i/P_0; \quad i = 25, 26, \ldots, N.$$

Normalization of rod position (R_i) is done by normalizing the overall change in the signal to a change of unity:

$$R_f = \frac{1}{L-K} \sum_{i=K}^{L} (R_i + 2.0); \quad 300 \leq K < L \leq 500;$$

$$R_i = [(R_i + 2.0) - R_f]/R_0,$$

where

$$R_0 = \frac{1}{24} \sum_{i=1}^{24} [(R_i + 2.0) - R_f].$$

Power and position values stored in the computer may consist of both positive and negative values; addition of OSV times gain to power and addition of 2.0 to the position data ensure that all values will be positive in the raw data, and the normalized values will then be of proper sign.

Normalization of power and position data to the average of the first 24 points for each ensures normalization to data acquired prior to motion of the rod during the test.

If it is deemed advisable, power data may be smoothed by a Hamming function,[8] a part of the computer code which normalizes the data and computes system reactivity and reactivity feedback.

4. Inverse-kinetics Determination of System Reactivity

Computation of system reactivity during the rod-drop experiment is accomplished by utilizing the customary one-group,[9-12] space-independent kinetics equations.

Begin with the equations:

$$\frac{dn(t)}{dt} = \frac{[\Delta k(t)(1 - \beta) - \beta]}{\ell^*} n(t) + \sum_{i=1}^{6} \lambda_i C_i(t); \tag{1}$$

$$\frac{dC_i(t)}{dt} = \frac{[1 + \Delta k(t)]}{\ell^*} \beta_i n(t) - \lambda_i C_i(t), \tag{2}$$

where

$n(t)$ = normalized neutron, or power, level at time t;

$\Delta k(t)$ = system reactivity at time t;

β_i = i^{th} delayed-neutron fraction;

λ_i = i^{th} delayed-neutron decay constant;

$C_i(t)$ = i^{th} delayed-neutron-precursor concentration at time t;

ℓ^* = prompt-neutron lifetime.

By combining Eqs. (1) and (2) we have

$$\frac{dn(t)}{dt} = \frac{\Delta k(t)(1-\beta) - \beta}{\ell^*} n(t) + \sum_{i=1}^{6} \lambda_i C_i(t) - \sum_{i=1}^{6} \frac{dC_i(t)}{dt}$$

$$+ \sum_{i=1}^{6} \frac{[1 + \Delta k(t)]}{\ell^*} \beta_i n(t) - \sum_{i=1}^{6} \lambda_i C_i(t).$$

Collecting terms results in the form

$$\frac{dn(t)}{dt} = \frac{\Delta k(t) n(t)}{\ell^*} - \sum_{i=1}^{6} \frac{dC_i(t)}{dt}. \qquad (1')$$

Linearize Eq. (2) by neglecting the product $\Delta k(t)\beta_i n(t)$, which is small compared with $\beta_i n(t)$; this results in the form

$$\frac{dC_i(t)}{dt} = \frac{\beta_i n(t)}{\ell^*} - \lambda_i C_i(t). \qquad (2')$$

Let $n(t)$ and $C_i(t)$ each be composed of a steady-state and a transient component:

$$n(t) = n_0 + \Delta n(t); \qquad C_i(t) = C_{i0} + \Delta C_i(t).$$

Consider Eq. (2') for the steady-state case:

$$\frac{d[C_{i0} + \Delta C_i(t)]}{dt} = \frac{\beta_i [n_0 + \Delta n(t)]}{\ell^*} - \lambda_i [C_{i0} + \Delta C_i(t)],$$

or

$$0 \approx \frac{\beta_i n_0}{\ell^*} - \lambda_i C_{i0} \qquad (3)$$

because the $\Delta n(t)$ and $\Delta C_i(t)$ are zero for the steady-state case and the derivative of a constant is zero.

Now Eq. (2') can be rewritten using Eq. (3):

$$\frac{d[\Delta C_i(t)]}{dt} = \frac{\beta_i \Delta n(t)}{\ell^*} - \lambda_i \Delta C_i(t). \qquad (2'')$$

Rewrite Eq. (1') with the Δ notation of Eq. (2"), and $\frac{dn_0}{dt} = 0$:

$$\frac{d[\Delta n(t)]}{dt} = \frac{\Delta k(t)[n_0 + \Delta n(t)]}{\ell^*} - \sum_{i=1}^{6} \frac{d[\Delta C_i(t)]}{dt} . \qquad (1")$$

The relation (2") can be solved by application of the integration factor $\exp(\lambda_i t)$ and evaluation of the integral in the resulting expression by trapezoidal integration:

$$\Delta C_i(t) = \frac{\beta_i}{\ell^*} \exp(-\lambda_i t) \int_{t_0}^{t} \Delta n(x) \exp(\lambda_i x)\, dx + \Delta C_i(t_0) \exp[-\lambda_i (t - t_0)]$$

$$= \frac{\beta_i}{\ell^*} \exp(-\lambda_i t) \frac{\Delta t}{2} [\Delta n(t_0) \exp(\lambda_i t_0) + \Delta n(t) \exp(\lambda_i t)] + \Delta C_i(t_0) \exp(-\lambda_i \Delta t);$$

$\Delta t = t - t_0$; in general $t_0 \neq$ time when $n = n_0$, $C_i = C_{i0}$.

Rearrange terms:

$$\Delta C_i(t) = \frac{\beta_i}{\ell^*} \frac{\Delta t}{2} [\Delta n(t_0) \exp(-\lambda_i \Delta t) + \Delta n(t) \exp(0)] + \Delta C_i(t_0) \exp(-\lambda_i \Delta t)$$

$$= \frac{\beta_i}{\ell^*} \frac{\Delta t}{2} [\exp(-\lambda_i \Delta t) \Delta n(t_0) + \Delta n(t)] + \Delta C_i(t_0) \exp(-\lambda_i \Delta t).$$

Substitute this expression for $\Delta C_i(t)$ in Eq. (2"), then substitute the resulting expression for $d\Delta C_i(t)/dt$ in Eq. (1"):

$$\frac{d\Delta n(t)}{dt} = \frac{\Delta k(t)}{\ell^*} [n_0 + \Delta n(t)] - \sum_{i=1}^{6} \frac{\beta_1 \Delta n(t)}{\ell^*} + \frac{\Delta t}{2} \sum_{i=1}^{6} \frac{\lambda_i \beta_i}{\ell^*} [\exp(-\lambda_i \Delta t) \Delta n(t_0)$$

$$+ \Delta n(t)] + \sum_{i=1}^{6} \Delta C_i(t_0) \exp(-\lambda_i \Delta t).$$

Multiply this relation by ℓ^* ($=10^{-7}$ sec) and neglect any term in which ℓ^* remains as a coefficient after reducing to lowest terms. The result is

$$0 = \Delta k(t)[n_0 + \Delta n(t)] - \beta \Delta n(t) + \frac{\Delta t}{2} \sum_{i=1}^{6} \lambda_i \beta_i [\exp(-\lambda_i \Delta t) \Delta n(t_0) + \Delta n(t)]$$

where

$$\beta = \sum_{i=1}^{6} \beta_i .$$

Solve this expression for $\Delta k(t)$:

$$\Delta k(t) = \frac{\beta \Delta n(t)}{n_0 + \Delta n} - \frac{\Delta t}{2[n_0 + \Delta n(t)]} \sum_{i=1}^{6} \lambda_i \beta_i [\exp(-\lambda_i \Delta t) \Delta n(t_0) + \Delta n(t)].$$

Multiply this expression by β^{-1} to obtain reactivity with units of dollars:

$$\Delta k(t) = \frac{\Delta n(t)}{n_0 + \Delta n(t)} - \frac{\Delta t}{2[n_0 + \Delta n(t)]} \sum_{i=1}^{6} \frac{\lambda_i \beta_i}{\beta} [\exp(-\lambda_i \Delta t) \Delta n(t_0) + \Delta n(t)]. \quad (4)$$

Equation (4) is used to evaluate the rod-drop worth at zero power and the system reactivity during rod-drop experiments at power. The $\Delta n(t)$ are obtained by normalizing the ion-chamber output to unity for the steady-state condition prior to the rod drop. Computing the appropriate values on the right side of the relation from the normalized power data is accomplished by considering that Eq. (4) represents the system reactivity at time t; the system reactivity is zero for t = 0. Pointwise change in reactivity due to the rod drop is computed from rod position at each time point and the value is subtracted from the system reactivity, leaving a value for system feedback reactivity.

B. Consideration of Error

Possible sources of error in the reactivity-measurement system include the position and characteristics of the neutron detector, neutronic noise, calibration of the electronics system, and data-reduction methods.

1. Neutron-detector Output

Location of the detector is not known to a precision necessary to examine the possibility of shielding effects on the ion-chamber signal. The chamber output current to preamplifier OA-1 (see Fig. 41) is linear with reactor power.

2. Neutronic Noise

Neutronic noise varies from run to run, with a maximum observed magnitude of about 4% of the measured neutron signal. Reduction of any error associated with neutronic noise is accomplished by means of several successive rod-drop experiments with pointwise averaging of computed results. In addition, power-data smoothing can be performed prior

to inverse-kinetics computations by use of a Hamming function--this option is provided in the computer code that performs the reactivity calculations.

3. Calibration of Electronics System

Calibration of the electronics system from operational amplifier OA-3 through the IBM-1620 computer (see Fig. 41) is subject to a variation of about 0.2% between minimum and maximum measured system gain. This uncertainty is carried in the power data.

4. Data-reduction Methods

The output of the A/D converter consists of digital values with a maximum of four significant decimal digits, ranging from -1.800 to +1.800. This implies an uncertainty as large as 0.001 due to truncation. The signal of interest here is the power signal. The resultant uncertainty in power data is, at most, 0.001/(minimum power) or about 0.001/0.8 = 0.0012, slightly more than 0.1% uncertainty, exclusive of any effects of noise in the data.

The inverse-kinetics computation is done with an IBM-360/75 system in double-precision arithmetic, so there is negligible error due to truncation or round-off. An error of 0.1% in power will give approximately 0.001$ error in computed system reactivity. The computation of reactivity feedback will additionally contain any error present in the calibrated worth of the drop rod.

Rod-worth calibration is determined from rod-drop experiments conducted at a reactor power level of 500 kW. Usually three or more experiments are pointwise averaged to obtain a rod-worth calibration. The calibration is assumed to be a continuous function of position. A measure of the uncertainty in the calibrated worth is the standard deviation between a smooth curve, fit to the calibration values, and the values themselves. Figures 42 through 47 show the best fits obtained for third- or fifth-order fits to the averaged calibrations used to compute reactivity feedback for the runs covered in this report. The standard deviation σ is given in the figure captions for the respective curve fits. Additionally, for the two sets of calibration data for run 33A, fits were made to each of these (unaveraged) sets of data. The best fit is shown in Fig. 46.

Note that the calibration of the low-worth rod (see run 36A, Fig. 47) should be fit only over the portion of rod travel occurring after the reactivity change becomes significant.

The inferred error in rod worth of the 0.05$ rod (runs prior to 35) is about 5%, which in turn implies that the error in the computed feedback can approach 0.0025$, plus or minus the 0.001$ error associated with the uncertainty in the power data.

No attempt is made here to separate noise effects completely from other effects, since the values for rod worth are sensitive to noise in the raw data.

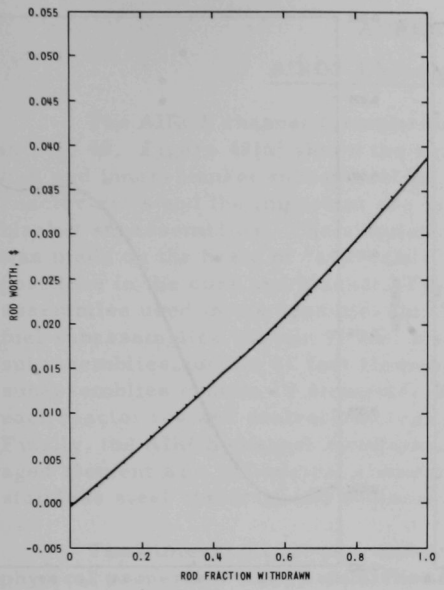

Fig. 42. Worth of Drop Rod in Run 26B, Third-order Fit

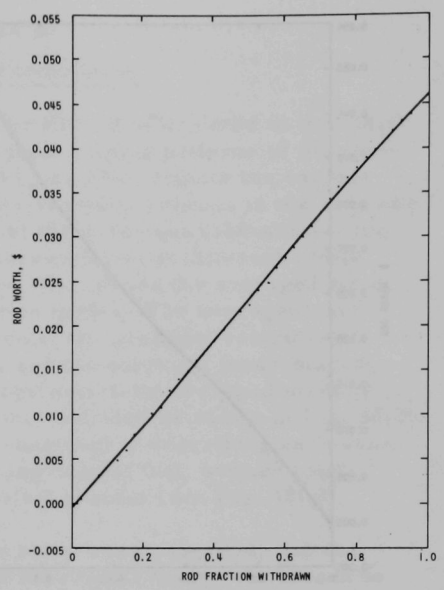

Fig. 43. Worth of Drop Rod in Run 29A, Third-order Fit

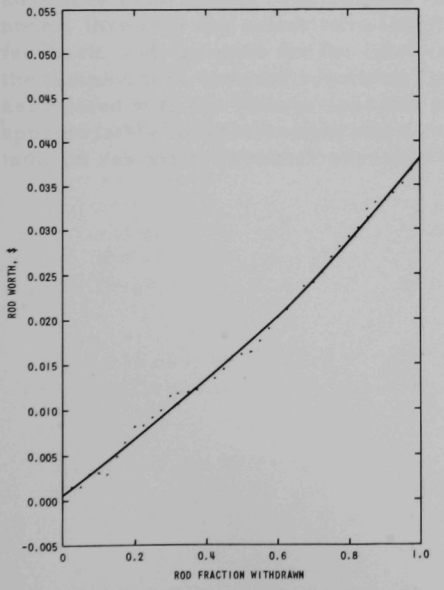

Fig. 44. Worth of Drop Rod in Run 29C, Third-order Fit

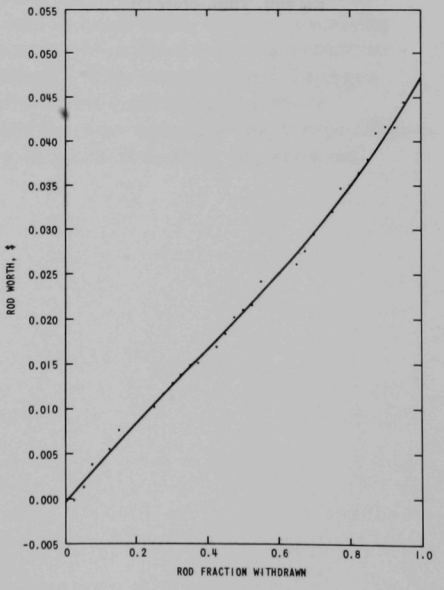

Fig. 45. Worth of Drop Rod in Run 33A (No. 2 control rod in), Third-order Fit

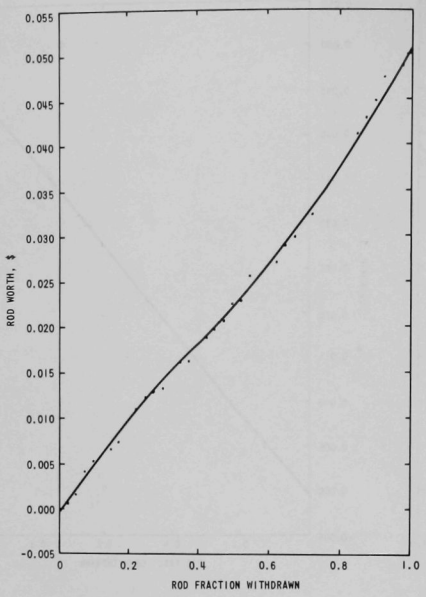

Fig. 46. Worth of Drop Rod in Run 33A (No. 2 control rod out), Third-order Fit

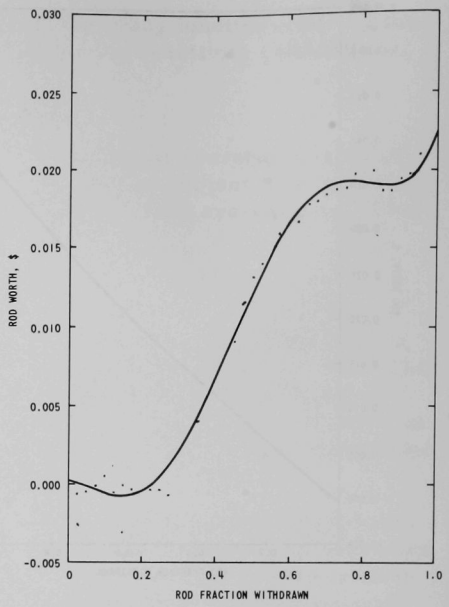

Fig. 47. Worth of Drop Rod in Run 36A, Fifth-order Fit

APPENDIX B

AIROS Channel Formulation

The AIROS channel formulation for EBR-II is depicted in five parts in Fig. 48. Figure 48(a) shows the hexagonal loading patterns of the core-fuel and inner-blanket subassemblies. Figure 48(b) depicts the various reactor rows and the important reactivity-feedback sources in the core and blanket subassemblies. The simulation of these various feedback sources was made on the basis of "averaged" subassemblies at different radial positions in the core and blanket. Figure 48(c) shows the averaged subassemblies used in the dynamic-simulation model. The averaged core-fuel subassemblies contain 91 fuel elements; the averaged control-rod subassemblies contain 61 fuel elements; and the averaged inner-blanket subassemblies contain 19 elements. A characteristic averaged element in each reactor row and control-rod region was selected as shown in Fig. 48(d). Finally, the AIROS channel simulations consisted of describing each averaged element as a cylindrical element composed of fuel, sodium bond, stainless steel cladding, and sodium-coolant annulus [see Fig. 48(e)].

The dimensions, power, and flow rates were computed; and the physical properties were established for all reactor materials chosen to represent the average temperature range of interest in each rod-drop experiment (see Appendix C). The fuel region was divided into three radial and three axial nodes. The coolant regions were divided into four axial nodes, three for the active core length, which contribute to the reactivity feedback, and one node for the inlet coolant, which does not contribute to the temperature-induced reactivity feedback. The temperature changes associated with the 96 heat-transfer nodes were multiplied by their appropriately weighed temperature coefficients to compute the temperature-induced reactivity feedback associated with each rod-drop experiment.

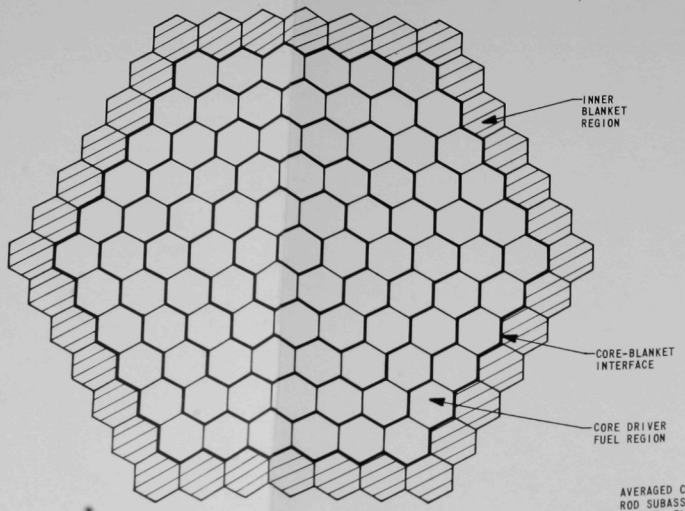

FIG. 48 (a)
GENERAL EBR-II CORE AND
INNER BLANKET CROSS-SECTIONAL CONFIGURATION

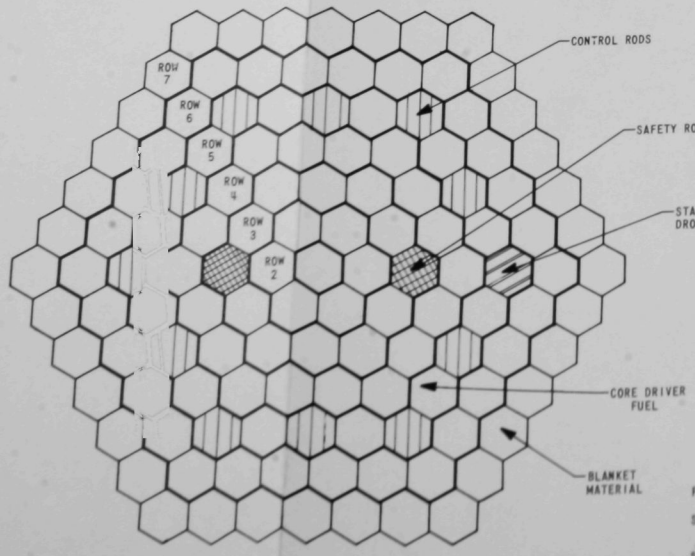

FIG. 48 (b)
PRINCIPAL TYPES OF REACTOR SUBASSEMBLIES
CONTRIBUTING REACTIVITY FEEDBACK

FIG. 48 (c)
"AVERAGED" SUBASSEMBLIES IN EACH REACTOR
ROW CONSIDERED IN REACTIVITY FEEDBACK

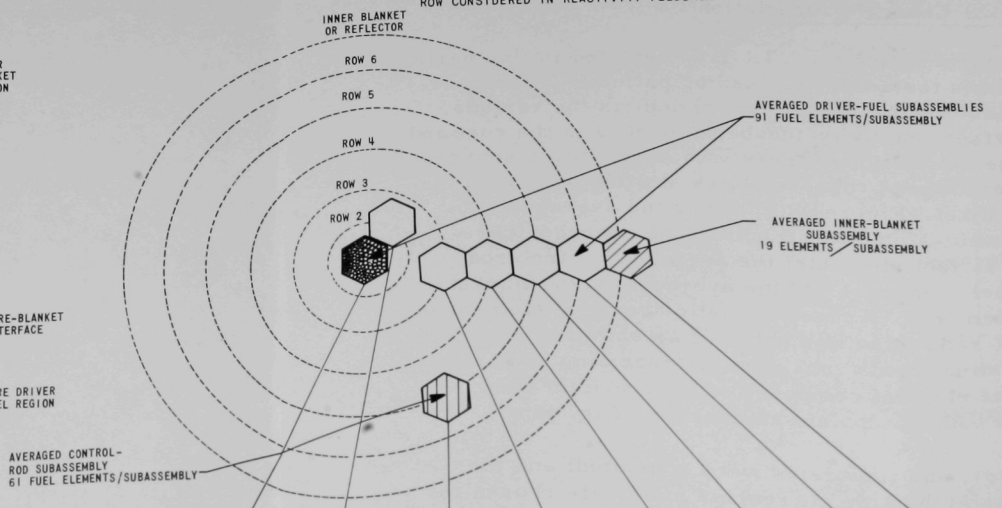

FIG. 48 (d)

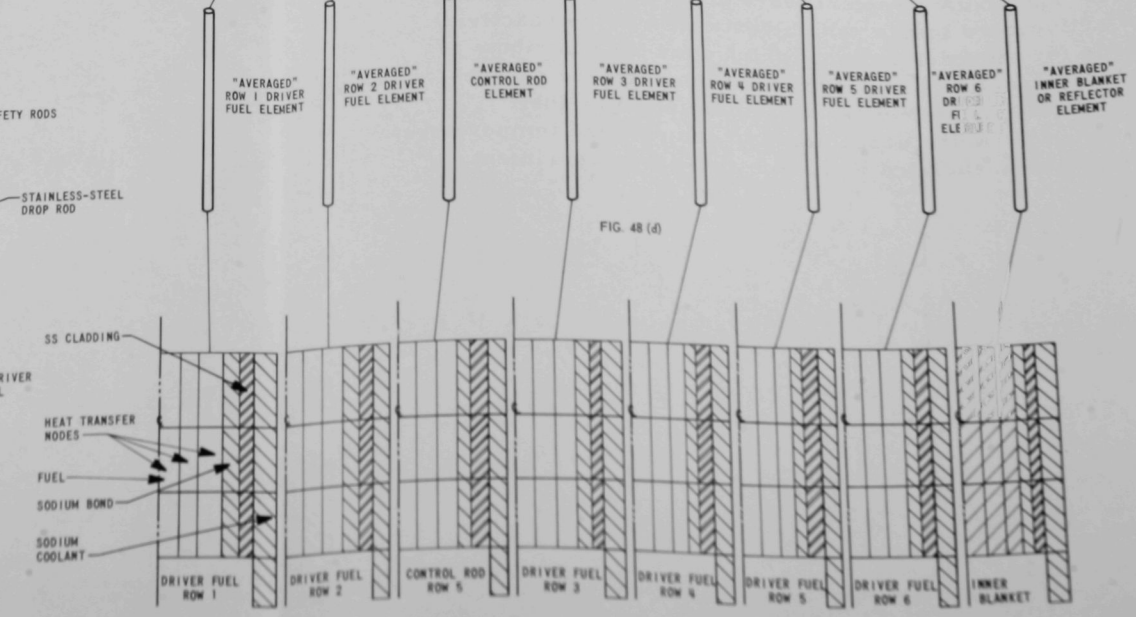

FIG. 48 (e)

Fig. 48. AIROS Channel Formulation for EBR-II Reactor

APPENDIX C

Physical Properties of Materials in Driver-fuel Elements

The transient response of EBR-II driver-fuel elements is partially dependent on the physical properties of the materials used in these fuel elements (i.e., uranium-5 wt % fissium, Type 304L stainless steel, and sodium). The physical properties of these reactor materials are all varying functions of the operating temperatures. In a rod-drop experiment the temperatures will decrease as negative reactivity is inserted into the reactor system. The amount of temperature decrease is dependent on the reactivity worth of the stainless steel drop rod and on the temperature-induced reactivity feedback of the system. Figures 49 through 54 show the thermal conductivities and specific heats of uranium-5 wt % fissium, Type 304L stainless steel, and sodium as functions of temperatures.

Table XIV lists the percentage changes in physical properties of reactor materials accompanying a decrease in operating temperature from the upper limit of 1200°F to the lower limit of 700°F.

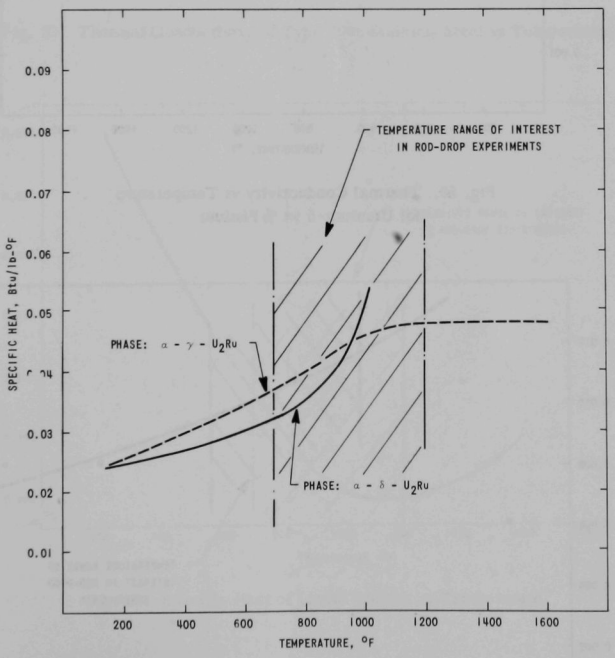

Fig. 49. Specific Heat vs Temperature for Uranium-5 wt % Fissium

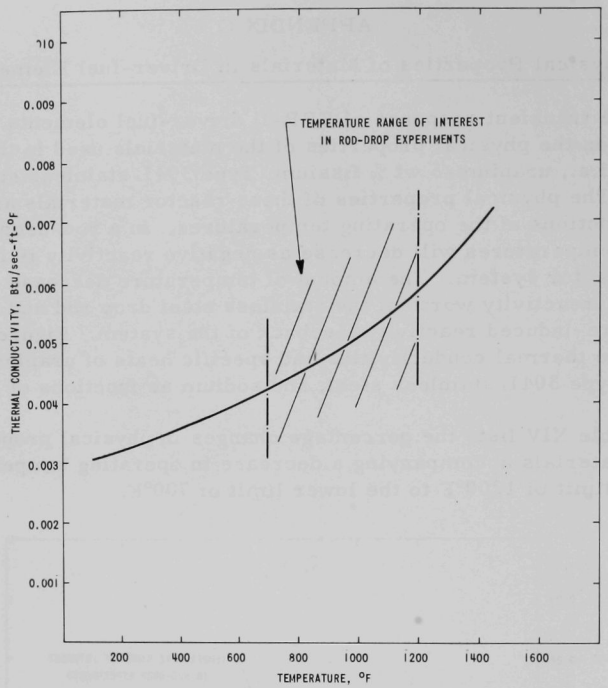

Fig. 50. Thermal Conductivity vs Temperature for Uranium-5 wt % Fissium

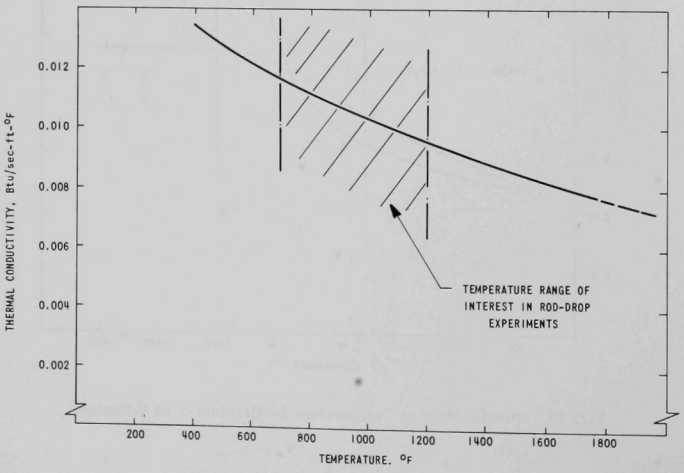

Fig. 51. Thermal Conductivity of Liquid Sodium vs Temperature

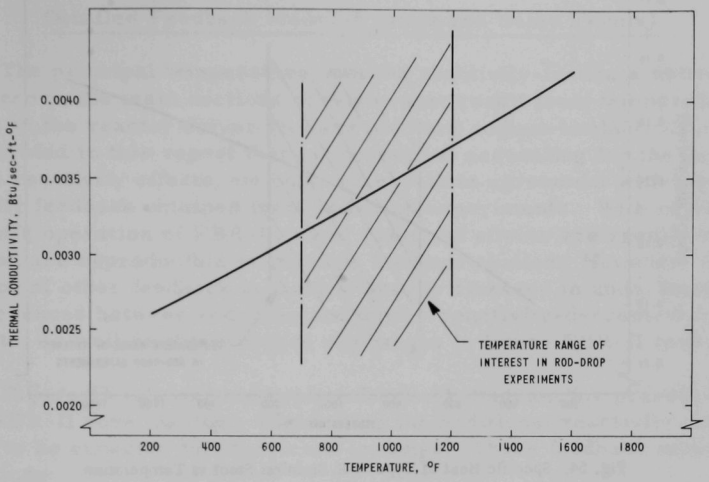

Fig. 52. Thermal Conductivity of Type 304L Stainless Steel vs Temperature

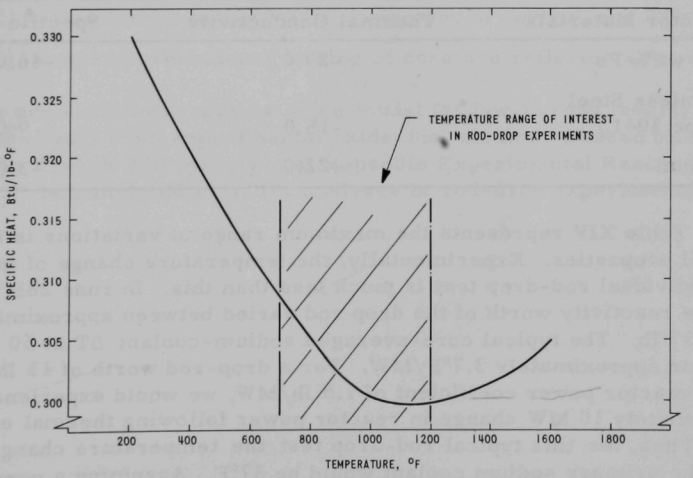

Fig. 53. Specific Heat of Liquid Sodium vs Temperature

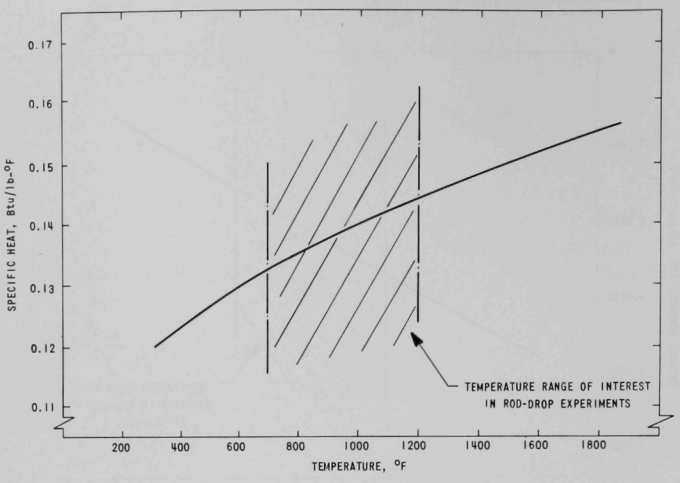

Fig. 54. Specific Heat of Type 304L Stainless Steel vs Temperature

TABLE XIV. Percentage Changes in Thermal Conductivity and Specific Heat of Reactor Materials (1200 to 700°F)

Reactor Materials	Thermal Conductivity	Specific Heat
U-5 wt % Fs	-29.0	-46.0
Stainless Steel (Type 304L)	-15.0	-9.0
Sodium	+22.0	+3.0

Table XIV represents the maximum range of variations in these physical properties. Experimentally, the temperature change of interest in an individual rod-drop test is much less than this. In runs 26B through 33A, the reactivity worth of the drop rod varied between approximately 12 and 17 Ih. The typical core-averaged sodium-coolant ΔT at 50 MW is 184°F, or approximately 3.7°F/MW. For a drop-rod worth of 15 Ih and a typical reactor power coefficient of 1.5 Ih/MW, we would experience an approximately 10 MW change in reactor power following thermal equilibrium. Thus, for this typical rod-drop test the temperature change in the ΔT of the primary sodium coolant would be 37°F. Assuming a nominal sodium-coolant temperature of 800°F, a drop of 37°F would change the thermal conductivity of the coolant by +1.0%. Therefore, the assumption of constant values for thermal conductivity and specific heat in each rod-drop experiment introduces a very small error. With the lower-worth drop rod, the error in the AIROS-IIA channel formulation is negligible.

APPENDIX D

Detailed Feedback Model (Prompt and Delay Terms)

The principal temperature-induced reactivity-feedback networks considered in the main sections of this report result from temperature changes in the reactor driver fuel and primary sodium coolant. It was demonstrated in this report that by theoretical accounting for the details of these reactivity effects, we obtained excellent agreement with measured reactivity feedback obtained from rod-drop experiments. With reference to the safe operation of EBR-II, these principal effects are readily understood and are reproducible in the core loadings studied. However, the existence of other feedback networks must be stressed in understanding the differences between rod-drop and power-reactivity-decrement measurements, as well as the influence of changes in future EBR-II core loadings.

Figure 55 is a more complete feedback diagram for present and future EBR-II core loadings, illustrating the additional reactivity contributions to be expected in future core loadings. These feedback networks will include:

(1) temperature-induced Doppler reactivity effects in experimental oxide fuel elements;

(2) temperature-induced axial expansion of control-rod drive shafts;

(3) temperature-induced bowing of core and reflector subassemblies.

In addition, there may be some initial (at low-burnup levels) fuel-expansion effects from experimental oxide-fuel elements, based on experience in the French FBR program at Rapsodie Experimental Reactor. These effects will be simulated in future analyses of rod-drop experimental results.

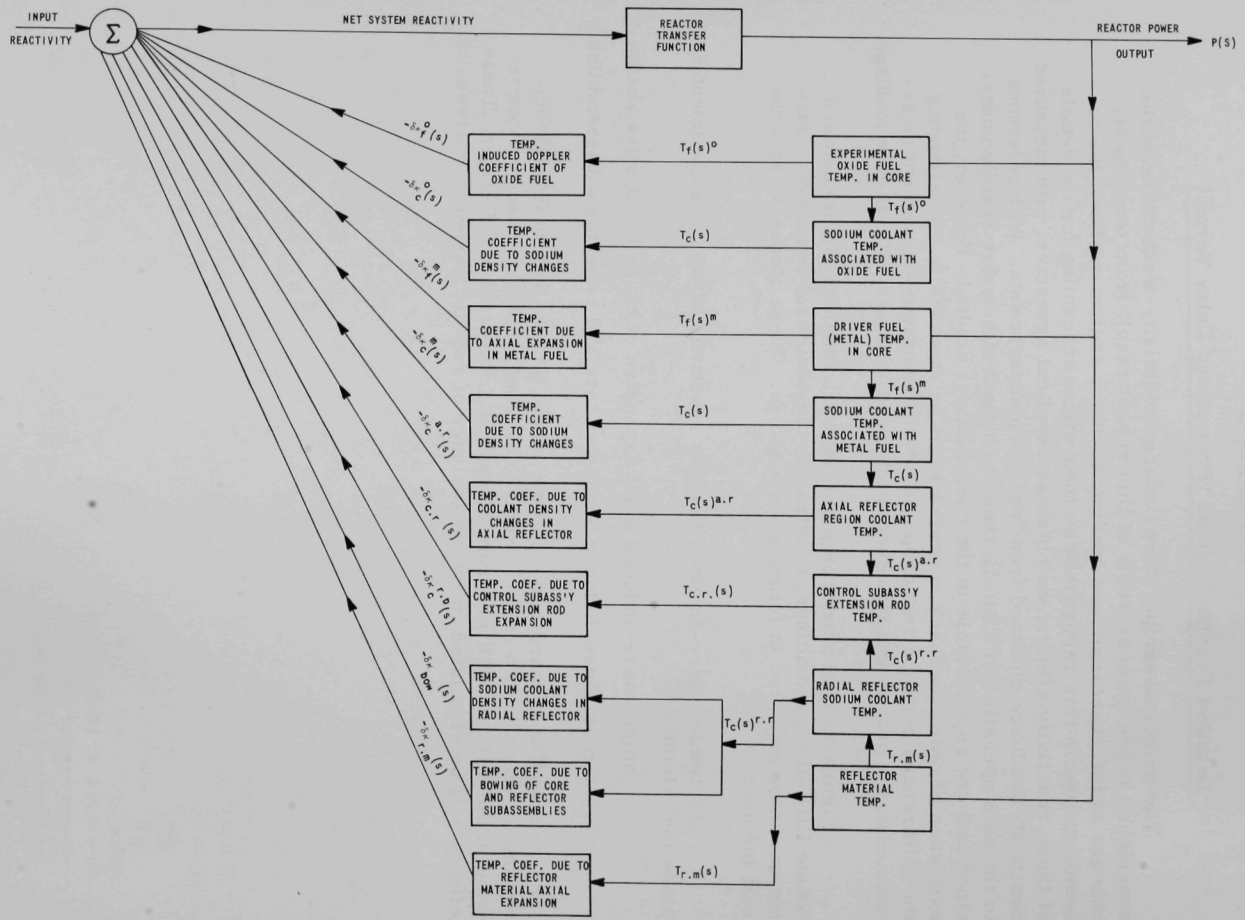

Fig. 55. Closed-loop Reactivity-feedback Networks for EBR-II Irradiation Cores

APPENDIX E

Proposed Instrumented Driver-fuel Subassembly*

An instrumented driver-fuel subassembly would appreciably enhance our ability to understand the dynamic behavior of EBR-II core loadings. Presently, only ion-chamber current is monitored and interpreted into relative changes in reactor power. As noted in Appendix A, the ion-chamber current is processed and converted into system reactivity. The dynamic-simulation model described in this report was used to analyze the results of these processed data. In computing the closed-loop feedback, temperatures in fuel, sodium bond, cladding, and coolant are calculated for each averaged fuel element in each row in the core and inner blanket.

An instrumented driver-fuel subassembly would provide detailed information on the temperature change in driver-fuel elements during a rod-drop experiment. A schematic representation of the EBR-II instrumented subassembly is given in Fig. 56. Figure 57 is a cross-sectional view of a typical subassembly loading, showing the locations of thermocouples and coolant flowmeters. The utilization of an instrumented driver-fuel subassembly in rod-drop experiments would greatly enhance our ability to detect temperature changes and would complement our present ion-chamber data. The combined data set would provide information pertaining to the detailed temperature-induced feedback networks required for a completed dynamic simulation and understanding of the EBR-II response.

*An instrumented subassembly containing experimental oxide-fuel elements is presently installed in the EBR-II core.

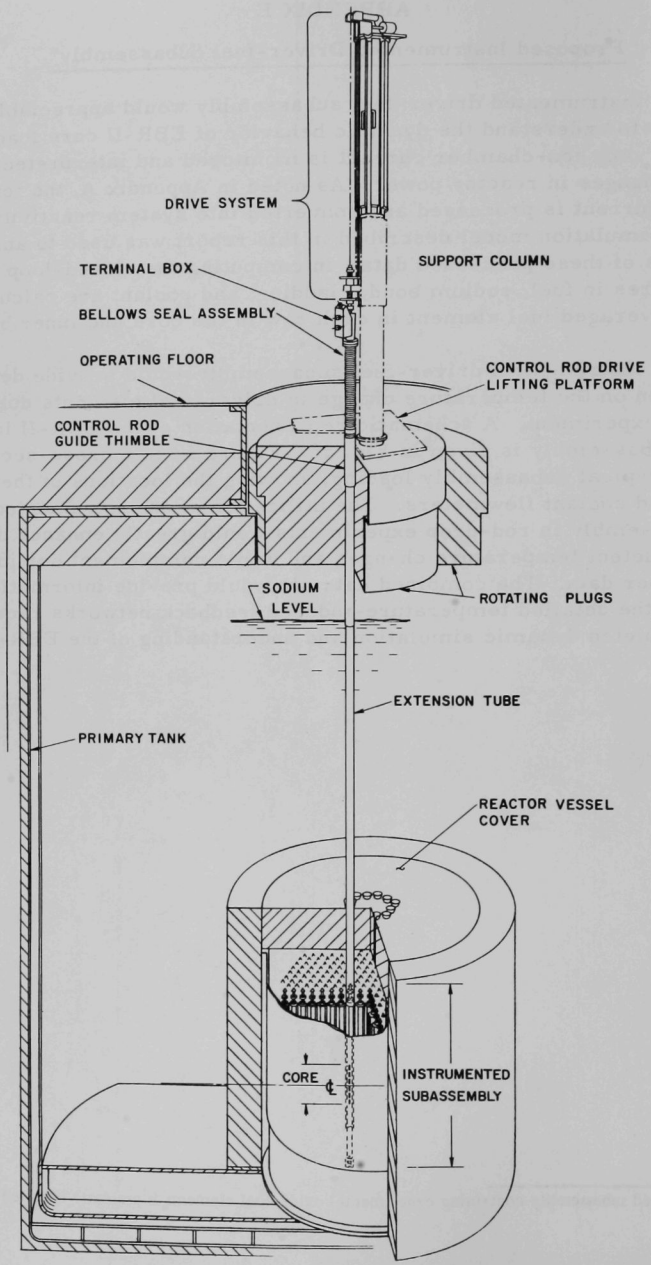

Fig. 56. Instrumented-subassembly Installation.
ANL Neg. No. 113-1608 Rev. 1.

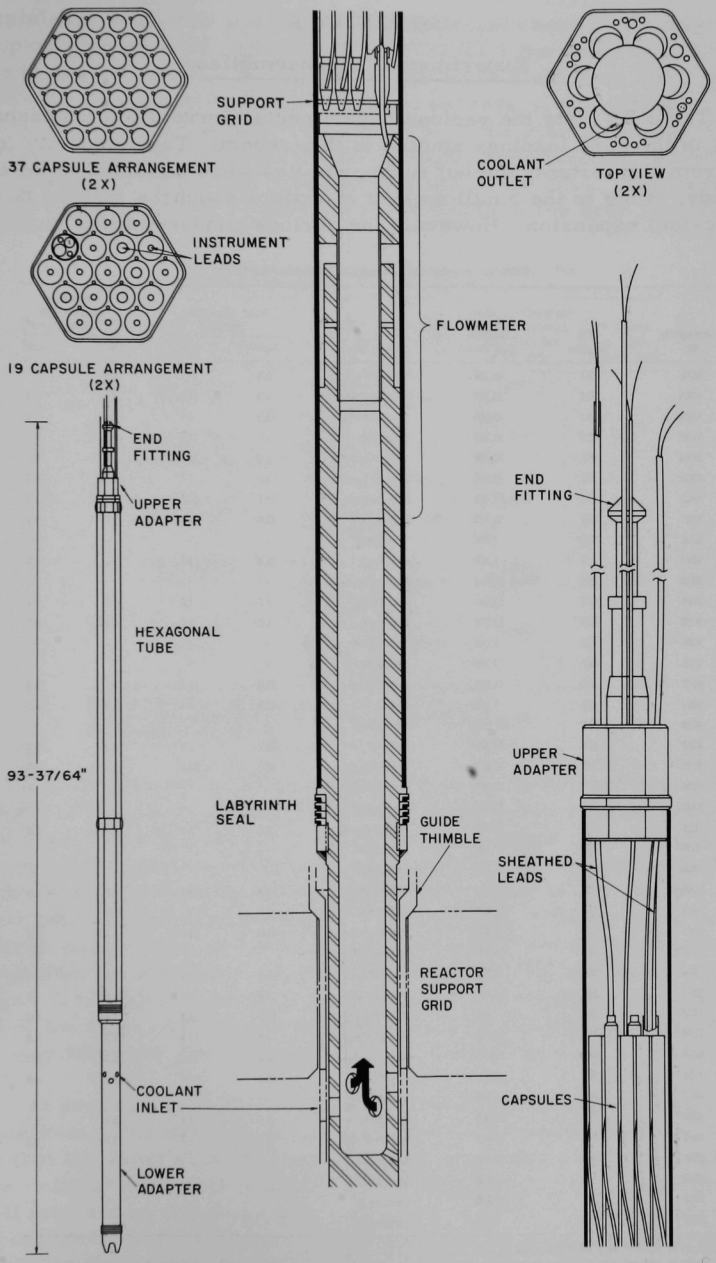

Fig. 57. Instrumented Subassembly. ANL Neg. No. 113-2409.

APPENDIX F

Experimental Subassemblies

Table XV lists the various experimental-irradiation subassemblies present in the core loadings studied in this report. The reactivity feedbacks from the ceramic-fueled subassemblies were assumed to be zero in this study, owing to the small amount of material and the lack of data on ceramic-fuel expansion. However, the various subassemblies surrounding

TABLE XV. Physical Characteristics of Irradiation Experiments

Subassembly No.	Grid Location	Exposure Goal (MWd)	Fuel Type	Power Generation (kW/ft)		Midplane Burnup Rate ([at. %/MWd] x 10^4)	
				Max[a]	Min[b]	Max[a]	Min[b]
XG02	7A1	16,700	UO_2-20 PuO_2	5.3	-	2.6	-
XG03	7D1	23,300	UO_2-20 PuO_2	5.3	4.6	2.6	2.4
XG04	7B1	45,000	UO_2-20 PuO_2	5.3	4.6	2.6	2.4
XG05	4C2	13,750	UO_2-PuO_2	15.5	13.5	6.1	5.5
XA08	4F2	20,700	$(U_{0.8}$-$Pu_{0.2})C$	26.0	17.2	6.2	4.2
X010	7F3	19,600	UO_2-20 PuO_2	8.6	7.7	3.7	3.3
X012	4B2	21,400	UO_2-20 PuO_2	15.5	13.5	6.1	5.4
X015	4A2	11,500	UO_2-PuO_2	15.4	14.0	6.1	5.6
X016	4D3	7,400	Structural[c]	-	-	-	-
X017	4C3	6,500	UO_2-PuO_2	15.4	13.5	6.1	5.4
X018	2B1	22,900	Structural	-	-	-	-
X019	6D2	13,000	UO_2-PuO_2	8.0	7.0	4.5	4.4
X020	6B5	13,000	UO_2-PuO_2	8.0	7.0	4.5	4.4
X022	7C4	5,000	Structural[c]	-	-	-	-
X025	4E2	7,700	Structural[c]	-	-	-	-
X027	4B3	16,000	UO_2-25 PuO_2	15.4	13.7	6.1	5.4
X029	4E3	5,100	U-5 Fs	10.2	8.4	5.9	4.5
X030	6E1	No Limit	Structural[c]	-	-	-	-
X032	6F1	14,300	PuO_2-25 UO_2	10.2	9.3	4.3	3.7
X033	5E2	12,200	$(U_{0.8}$-$Pu_{0.2})C$	22.2	18.0	5.3	4.7
X034	2F1	14,800	Structural[c]	-	-	-	-
X035	7B4	44,800	Structural[c]	-	-	-	-
X036	7E1	33,300	UO_2-25 PuO_2	8.2	6.0	2.7	2.0
X038	7C5	17,700	Structural[c]	-	-	-	-
X900	7A4	2,700	Structural[c]	-	-	-	-
X040	5B2	7,000	UO_2-PuO_2	16.4	14.4	4.9	4.5
X041	7A3	16,700	Structural	-	-	-	-
X043	4D2	6,100	UO_2-25 PuO_2	16.5	14.0	5.5	4.9
X044	7A1	8,100	Structural[d]	-	-	-	-
X050	4C2	7,500	UO_2-PuO_2	15.2	13.6	5.6	5.1
X051	3A2	16,400	UO_2-25 PuO_2	6.0	5.7	2.0	1.9
X053	4E3	3,600	U-5 Fs	10.2	8.4	5.4	4.0
X054	4E1	10,000	UO_2-25 PuO_2	15.2	13.7	5.3	4.8
X055	6A4	20,000	$(U_{0.85}$-$Pu_{0.15})C$	14.2	13.4	3.2	2.7
X056	5C2	10,600	UO_2-25 PuO_2	13.6	12.4	5.0	4.3
X057	2B1	15,000	Structural[c]	-	-	-	-
X058	7F3	16,000	UO_2-25 PuO_2	9.5	7.7	3.5	2.7
X059	4A1	17,500	UO_2-25 PuO_2	9.6	9.1	3.4	3.2
X060	7C3	5,400	Structural[c]	-	-	-	-
X061	7A5	18,000	Structural[c]	-	-	-	-
X063	7F5	5,400	Structural[c]	-	-	-	-
X067	4A3	2,400	Structural[c]	-	-	-	-

[a]Capsule or element with maximum value.
[b]Capsule or element with minimum value.
[c]Structural tests of cladding materials (i.e., 304L, 316, V-20 Ti, Hast-X, INCO-625, etc.).
[d]Structural tests of materials (i.e., Al_2O_3, Y_2O_3).

the stainless steel drop rod may be the principal cause of the uncertainty in drop-rod worth at full power. Table XVI lists the subassemblies in the first and second rings surrounding the stainless steel drop rod. The second ring of subassemblies is included because of experimental data obtained in run 33A. In this run, the worth of the stainless steel drop rod was measured at 500 kW with the No. 2 control rod (second ring) in the core and again with the No. 2 control rod out of the core. The results of this experiment showed a decrease in the worth of the drop rod of 6.6%.

TABLE XVI. Changes in Local Environment Surrounding the Stainless Steel Drop Rod and Associated Reactivity-worth Changes for the Drop Rod

Run No.	Nearest Subassemblies to Stainless Steel Drop Rod (not driver fuel)	Second Ring of Subassemblies Influencing Worth of Stainless Steel Drop Rod	Measured Reactivity Worth of Stainless Steel Drop Rod at 500 kW($)	% Change in Worth between Runs
26B	X019 (Oxide and Carbide Fuel)	XG03 (Oxide Fuel) Reflector (Stainless Steel) X017 (Oxide Fuel)	0.0417	-
29A	X019 (Oxide and Carbide Fuel) Blanket (Depleted Uranium)	XG03 (Oxide Fuel) X016 (Oxide Fuel) X017 (Structural) Reflector (Stainless Steel)	0.0493	+18.2
29C	X019 (Oxide and Carbide Fuel)	XG03 (Oxide Fuel) Blanket (Depleted Uranium) X016 (Structural) X017 (Oxide Fuel)	0.0408	-20.8
33A	X019 (Oxide and Carbide Fuel)	X038 (Structural) Blanket (Depleted Uranium) XG03 (Oxide Fuel) X043 (Oxide Fuel)	0.0533 (0.0500)[a]	+30.6 (-6.6)[b]
36A	X019 (Oxide and Carbide Fuel)	X038 (Structural) Blanket (Depleted Uranium) XG03 (Oxide Fuel) X043 (Oxide Fuel)	0.0221[c]	-

[a]Worth of stainless steel drop rod with No. 2 control rod out of core.
[b]Change in worth of stainless steel drop rod due to withdrawal of No. 2 control rod.
[c]New low-worth stainless steel rod.

Early work by R. W. Hyndman and R. B. Nicholson[2] deduced that the worth of the stainless steel rod changed when the reactor power was raised from 500 kW to 45 MW. Since a large number of small changes occur in raising the reactor power, it is difficult to separate effects. The effective material density of the reactor decreases as the reactor power is increased, thereby increasing neutron leakage. The increase in temperatures causes the core-fuel subassemblies to bow outward because of induced thermal gradients, thereby increasing radial and axial neutron leakage. If changes in neutron leakage affect the at-power reactivity worth of the stainless steel drop rod, then the surrounding subassemblies could also influence the reactivity worth of the drop rod.

At present, only limited data are available to resolve this important question. The existing experimental data presented in Table XVI imply that the local environment does influence the worth at 500 kW. Future critical assemblies in ZPR-3 and additional power experiments in EBR-II may aid in resolving this question. Our ability to interpret changes in the dynamic characteristics of any given core loading is dependent on our knowing the reactivity worth of the drop rod.

REFERENCES

1. R. A. Blaine and R. F. Berland, "A Description of AIROS IIA" in *Simulation of Reactor Dynamics*, Vol. 1, NAA-SR-12452 (Sept 1967).

2. R. W. Hyndman and R. B. Nicholson, *The EBR-II Feedback Function*, ANL-7476 (July 1968).

3. J. A. DeShong, Jr., *Dynamic Analysis of Liquid-metal-cooled Fast Power Reactors*, ANL-7529 (Jan 1969).

4. *Reactor Development Program Progress Report October 1968*, ANL-7513, pp. 46-47.

5. W. P. Keeney and J. K. Long, "Zero-Power Reactor III (ZPR-III)" in *Idaho Division Summary Report July, August, September 1960*, ANL-6301, pp. 45-77.

6. W. R. Wallin, F. D. McGinnis, J. F. Koenig, and V. G. Eschen, *EBR-II Subassembly Coolant-outlet Temperature Measurement*, Trans. Am. Nucl. Soc. *12*(2), pp. 806-808 (Nov 1969).

7. R. R. Smith, T. R. Bump, R. A. Cushman, R. W. Hyndman, F. S. Kirn, W. B. Loewenstein, J. K. Long, J. T. Madell, P. J. Persiani, and W. R. Wallin, *The Effects on an Over-cooled Stainless Steel Reflector on the EBR-II Power Coefficient*, ANL-7544 (May 1969).

8. R. B. Blackman, *Linear Data Smoothing and Prediction in Theory and Practice*, Addison-Wesley Publishing Co., Reading, Mass. (1965), p. 136.

9. Samuel Glasstone and Alexander Sesonske, *Nuclear Reactor Engineering*, D. Van Nostrand Co., Princeton, N. J. (1963).

10. G. Robert Keepin, *Physics of Nuclear Kinetics*, Addison-Wesley Publishing Co., Reading, Mass. (1965), p. 322.

11. R. O. Brittan, *Some Problems in the Safety of Fast Reactors*, ANL-5577 (1956), p. 5.

12. L. E. Weaver, *Systems Analysis of Nuclear Reactor Dynamics*, an AEC monograph, Rowman & Littlefield, Inc., New York (1963).